Responses to Reviewers for "Arctic observations and numerical simulations of surface wind effects on Multi-Angle Snowflake Camera measurements"

Kyle E. Fitch[1,2], Chaoxun Hang[3,4], Ahmad Talaei[1], and Timothy J. Garrett[1]

[1]Department of Atmospheric Sciences, University of Utah, Salt Lake City, 84112, USA
[2]Department of Engineering Physics, Air Force Institute of Technology, Wright-Patterson Air Force Base, Ohio, 45433, USA
[3]Department of Civil Engineering, Monash University, Clayton, 3168, Australia
[4]School of Oceanography, Shanghai Jiao Tong University, Shanghai, 200240, China

Correspondence: Kyle Fitch (kyle.fitch@afit.edu)

1 Reviewer #1

The subject of the well written and structured paper is well within the scope of AMT as it provides new tools and data for the correct use of an (already established) instrument for snowflake measurements called "Multi-Angle Snowflake Camera“ (MASC). For this purpose, the authors use a combination of numerical simulations based on an Euler-Lagrange approach and field based measurements. The main findings are guidelines for the correct usage of the above mentioned MASC, which I consider a substantial contribution to further investigations of snowfall measurements. Event though the article is quite good in my opinion and I would not argue with the main findings, I have some remarks. (Disclaimer: Please note that I am not an expert in precipitation measurement and my expertise mainly is in fluid and particle dynamics and the simulation thereof. So if there are points regarding especially the meteorological topics that I did not get right, please do not hesitate to object/improve.)

Major remarks:

1) The description of the CFD simulation setup should be a bit more detailed: What is the total number of cells? (Table 1 seems to give a wrong information about this, as the cells would be much larger as they seem in Figures 1(c)-1(e)) Have there been any examinations on grid independency?

We have added more details to the description as follows (note Table 2 corresponds to Table 1 in the original manuscript):

“The *snappyHexMesh* tool requires an existing base mesh to work with, which is generated from *blockMesh* and is represented in Table 2. For *snappyHexMesh*, two of the most important parameters are *nCellsBetweenLevels*, set to 3, and the *refinementSurfaces* level, which is set to a minimum of 4 and maximum of 5. This brings the total number of cells to 131,864 when the block is $4\ \mathrm{m} \times 4\ \mathrm{m} \times 5\ \mathrm{m}$. These values were determined through analysis of grid independence. For *blockMesh*, the resolution of $25\ \mathrm{cm} \times 25\ \mathrm{cm} \times 25\ \mathrm{cm}$ provided the most efficient mesh for a fixed *snappyHexMesh*. The *snappyHexMesh* parameters were also determined through testing; lower values (e.g., *nCellsBetweenLevels* < 3 or *refinementSurfaces* level < 4) rendered the mesh too coarse to capture the interaction between particles and flow inside of the aperture, while larger values come at a much higher computational cost.”

Please specify the boundary conditions.

We have added the following specifications to the simulation description:

“The boundary conditions for velocity include a flat velocity profile at the inlet; slip conditions at top, bottom, front, back and outlet surfaces; and a no-slip condition at the object (MASC). Zero gradient pressure fields are applied at all boundaries.”

Please justify why potentially important forces acting on particles in turbulent/shear flows are neglected (lift force, pressure gradient force)

We have rearranged the sections and wording in the title (as suggested by Reviewer #2) to reflect that the observations analysis is the featured part of our work, and that the relatively simple simulations serve only a supporting role. We have added the following to the conclusions section:

“Relatively simple simulations were carried out here to support the findings of the observations analyses. We used only a single set of particles with limited, yet representative characteristics to support observations analyses with simulated particle responses to MASC-perturbed flow. Future work could include a much more diverse set of particle shapes, sizes, and densities, as well as a turbulent dispersion model and other forces that have been neglected in this work.”

Where are the starting positions of the particles? (could be included e.g. in one of the figures 1(c)-1(e))

We have expanded the description of initial positions in the text (and added a new figure showing simulated particle trajectories) as follows:

“The particles fall downward at an initial velocity of $1\,\mathrm{m\,s^{-1}}$ from an initial height of $3\,\mathrm{m}$ above the MASC in the $-z$ direction under the force of gravity, reaching an average terminal velocity of $1.05\,\mathrm{m\,s^{-1}}$ well before encountering flows perturbed by the MASC. Initial particle positions are ∼2 to 20 m away from the MASC in the upstream horizontal direction, depending on the flow velocity. These initial positions were evaluated to ensure the particles fell into the center of the aperture. An example of simulated particle trajectories is shown in Fig. 12.”

2) Furthermore, I would suggest using more particles and particles of different size and shape according to the different riming classes seen in the measurements. And, as the influence of turbulent wind on the collection characteristics is examined, a model for turbulent dispersion should also be included. The finding that fall velocity is reduced with increasing wind speed could maybe have been made without the particle simulation part by just looking at the fluid velocities inside/above the collection area. If so, the particle simulations might as well be left out and more detailed particle simulations would be something for further work.

Although we neglect some of the details as you point out, we feel that it is still necessary to show the influence of the perturbed flow on the mean fall speed of a set of particles with which to compare the MASC measurements. As stated above in response to #1, we have rearranged the sections (as suggested by Reviewer #2) and wording in the title to reflect that the observations analysis is the featured part of our work, and that the relatively simple simulations serve only a supporting role. We have added the following to the conclusions section:

"Relatively simple simulations were carried out here to support the findings of the observations analyses. We used only a single set of particles with limited, yet representative characteristics to support observations analyses with simulated particle responses to MASC-perturbed flow. Future work could include a much more diverse set of particle shapes, sizes, and densities, as well as a turbulent dispersion model and other forces that have been neglected in this work."

3) As in principle the dependence of the collection efficiency on particle dynamic properties is investigated, I would suggest to include some thoughts on and references to general particle dynamics. Namely, there is the particle Stokes number, defining the ability of particles to respond to sudden changes in the carrier fluid's velocity. It is proportional to the product of particle density and the square of the diameter. Aggregates with comparatively low densities would have a low Stokes number, indicating that they follow the flow better than more dense aggregates. Additionally, bodies moving through fluids tend to orient in a manner that the drag is maximised. For oblate particles this would mean that their "plane" is oriented perpendicular to the flow direction. With these two principles a lot of the paper's findings can be explained quite well.

We have added the following to the discussion section (note that Figs. 8 & 6 and Table 1 correspond to Figs. 12 & 10 and Table 3 in the original manuscript, respectively):

"Larger aggregates with negligible riming tend to be more susceptible than smaller, more dense particles to disturbance by surface winds and associated turbulence, with a tendency for more vertical orientations (Fig. 8), slower fall speeds (Fig. 6), and with a lower frequency of occurrence at higher wind speeds (Table 1) than for other riming classes. The Stokes number is defined as the dimensionless ratio of the particle relaxation time to its terminal velocity in still air v_t/g, and a characteristic time of isotropic, homogeneous turbulent flow. Snowflakes with low Stokes numbers tend to follow the flow, becoming trapped in the vortices with the orientation aligning with the local velocity gradient (Voth & Soldati, 2017). The implication is that large, low-density, aggregate-type hydrometeors — with relatively small values of v_t compared to more heavily rimed particles — have low values of the Stokes number and are more likely to follow the motions of any turbulent flow induced by the MASC aperture. This finding is consistent with prior work by Thériault et al. (2012) who showed that for a Geonor gauge inside a single Alter shield, higher-density, faster-falling hydrometeors are collected most efficiently."

Voth, G. A., & Soldati, A. (2017). Anisotropic particles in turbulence. Annual Review of Fluid Mechanics, 49, 249-276. https://doi.org/10.1146/annurev-fluid-010816-060135

4) Regarding the orientation of particles: As non-spherical particles tend to arrange themselves in some preferential angle to the flow, the concept of determining their orientation seems questionable even for medium wind speeds between 1.5 m/s and 5.0 m/s, as the flow above and inside the measurement region seems to be heavily influenced by the device. What are the authors' views on this?

This is why we deemed it necessary to show orientations in even lighter winds (i.e., wind speeds as low as $< 0.5\,\mathrm{m\,s}{-1}$ in Fig. 12 from the original manuscript). This figure shows not only what the preferred orientation angle is such light winds, but also how sensitive the larger, low-density aggregates are.

Minor remarks:

Section 1: L46f: suggested change from "characterize" to "were used to characterize" or similar

Fixed as suggested

L58f: Isn't the collection region cylindrical or circular, not ring-shaped?

This has been changed to a "hollow, decagonal-prism-shaped collection volume" to more accurately describe the shape of the collection region.

L58ff: I would suggest to include some information about the different parts' positions in Fig. 1a)

Added information about parts' positions as follows:

"The system's casing houses three cameras focused on a point at the center of the collection volume 10 cm away, with each camera separated by 36° (for more details, see Fig. 1 from Garrett et al., 2012). A coupled system of directly opposing near-infrared emitters and detectors, vertically separated by 32 mm, detects falling hydrometeors larger than $\sim$0.1 mm in maximum dimension (Garrett and Yuter, 2014). This triggers the cameras and three high-powered LEDs located directly above on top of the casing."

L70ff: Maybe the number of references can be reduced, where possible?

We removed all Garrett et al. references that had already been cited and added "e.g.," to show that this is a subset of relevant references.

L90f: also include influence on riming degree among "fall speed, fall orientation, and size distribution"?

Added as suggested

Section 2: Please specify more clearly: It seems that first a steady state simulation with simple-Foam is done, and afterwards particles are tracked through a "frozen" flow field, but it is not actually mentioned.

The following statement was added to the CFD description: "The flow is allowed to reach steady-state prior to tracking particles through a 'frozen' flow field."

L96: Which solver? Maybe simpleFoam should be mentioned here already.

Wording in this paragraph has been rearranged to correct this and mention simpleFoam earlier.

L100: simpleFoam instead of simpleFOAM

Corrected

L115: Please specify the drag coefficient function.

We have updated the text to state, "The drag coefficient $C_D(Re_p)$ is defined as $C_D = (24/Re_p)(1 + Re_p^{2/3}/6)$ for $Re_p \leq 1000$ and $C_D = 0.44$ for $Re_p > 1000$"

L115 & L117: Re should be Re_p

Corrected

Fig. 2: I would suggest writing "wind directions" instead of "wind vectors". What crosssection is meant? Maybe the plane for the arrows? Please specify. A more detailed view of the results inside/around the measurement section would be nice, as it would be possible to examine the wind speed there more detailed. Is it possible to show some exemplary particle path lines? (additional images could be included as supplementary material)

We have updated the caption to state:

“Simulated wind field around the MASC with undisturbed winds set at $1\,\mathrm{m\,s^{-1}}$ towards the +y direction. Color represents the vertical wind speed v_{f_z}, and arrows show wind directions on the y–z plane. The plane in which the arrows are located is aligned with the center of the aperture on the y–z plane, and x–positive points out of the page.”

In response to the request for a figure showing examples of particle trajectories from two reviewers, we have added an appendix with four figures to the revised manuscript.

Fig. 3 and Fig. 4: Please indicate where the data is sampled.

We have added the statement, “Data are sampled at the center of the aperture” to each of these captions.

L130: “in the k-ω-SST closure model”

Corrected

Section 3: L137: “the angle between D_{max} and the local horizontal” should be “the angle between the major axis and the local horizontal”

Corrected as suggested and also clarified the definition of maximum dimension in the preceding sentence to say that it is defined as the length of the major axis

L143: Is the average of the three images the best guess for the actual orientation angle? How “stable” is the detection of orientation angles for rimed particles, as they might have no clear major axis?

We have added to the discussion section:

“An average is not the best guess for the true orientation angle in all cases. For example, depending on the azimuthal orientation with respect to the central camera, the particle’s major axis may not be resolved entirely. Jiang et al. (2019) showed that the azimuthal orientation is correlated with the wind direction, with particles’ major axes tending to align with the wind direction. In our case, this would imply that the major axis was often oriented such that it was not entirely resolved by any of the three cameras. More work needs to be done to investigate the limitations of the MASC-determined orientation angle.”

Fig. 6(b) might be dropped in my opinion

We have decided to keep this as no other reviewers commented on it, and we feel it adds some clarification through an additional perspective

L171: Why were the PDFs adjusted with a Gaussian kernel and how do the original data look?

Added to the end of the Hydrometeor observations – methods section:

Results are presented here in the form of probability density function (PDF) estimates, calculated using a kernel density estimator of the form

$$\hat{f}(x_0) = \frac{1}{n_s h} \sum_{i=1}^{n_s} K\left(\frac{x_0 - x_i}{h}\right) \tag{1}$$

where x_0 is a real value of the distribution being estimated, x_i is a random sample from the distribution, n_s is the sample size, and h is the bandwidth (Wilks, 2011). The Gaussian smoothing function is $K(x) = (2\pi)^{-1/2}\exp(-x^2/2)$ for a random variable x, and h is optimized according to Bowman & Azzalini (1997) to produce a smooth curve.

Table 3: In the regime of $U_{sfc} \leq 5\,m/s$: Are the data for smaller U_{sfc} also contained in values for larger U_{sfc}? (e.g. is the data of $U_{sfc} \leq 0.5\,m/s$ also in $U_{sfc} \leq 1.0\,m/s$?)

Yes and we have added the following clarification to the table's caption: "Less restrictive wind speed categories (e.g., $\leq 5\,\mathrm{m\,s^{-1}}$) include data from more restrictive categories (e.g., $\leq 1.5\,\mathrm{m\,s^{-1}}$)"

L187f: If something different is simulated, then it should not be compared to that. There seems to be a significant difference between the measurements and the simulations. Please include some discussion about this difference.

This comparison statement has been removed and the following paragraph has been added to the discussion:

"For unshielded MASC measurements, the simulations show that the separation of flow leads to an upward flow velocity component above the aperture that tends to decrease the mean fall speed of particles falling into the aperture (Figs. 14 and 15). As wind speed increases, the mean simulated fall speed decreases, and values do not deviate substantially from the mean (Figs. A1 through A4). In contrast, unshielded measurements of fall speed are highly skewed towards low values (Figs. 5(a) and (b)) and the distribution is bimodal for the lightest winds (Fig. 5(c)). Therefore, while the primary effect of perturbed winds slowing particle fall speeds is generally well represented in the simulations, the details appear to be more complicated in reality."

Fig. 10: The low fall speed mode seems to be less prominent ($U_{sfc} <= 1.0$ and $1.5\,m/s$) or even vanishes ($U_{sfc} <= 0.5\,m/s$) for aggregates. Is there any explanation for this?

It is not clear to us why this is the case. One idea is that the spectrum of aggregate fall speeds is less susceptible to broadening by turbulent eddies, but this would need to be investigated in a separate work.

Section 4: As metioned above, please include some discussion of the simulation results and how they compare to the measurements. As mentioned in major remarks, I suggest including some of these thoughts: Falling objects tend to orient in maximum drag conditions, which matches the findings here. (compare L196ff) As aggregates seem to have smaller fall velocities than particles of the other two categories, they should be oriented more vertical to orient in maximum drag conditions when experiencing the same horizontal wind speeds. This again matches with the findings. (compare L201) Aggregates are more prone to get blown away by the surface winds as they have comparatively low Stokes numbers and high surface-to-density-ratios in comparison to more rimed particles. (compare L205ff)

As mentioned above, we have added the following to the discussion section (note that Figs. 8 & 6 and Table 1 correspond to Figs. 12 & 10 and Table 3 in the original manuscript, respectively):

"Larger aggregates with negligible riming tend to be more susceptible than smaller, more dense particles to disturbance by surface winds and associated turbulence, with a tendency for more vertical orientations (Fig. 8), slower fall speeds (Fig. 6), and with a lower frequency of occurrence at higher wind speeds (Table 1) than for other riming classes. The Stokes number is defined as the dimensionless ratio of the particle relaxation time to its terminal velocity in still air v_t/g, and a characteristic time of isotropic, homogeneous turbulent flow. Snowflakes with low Stokes numbers tend to follow the flow, becoming trapped in the vortices with the orientation aligning with the local velocity gradient (Voth & Soldati, 2017). The implication is that large, low-density, aggregate-type hydrometeors — with relatively small values of v_t compared to more heavily rimed particles — have low values of the Stokes number and are more likely to follow the motions of any turbulent flow induced by the MASC aperture. This finding is consistent with prior work by Thériault et al. (2012) who showed that for a Geonor gauge inside a single Alter shield, higher-density, faster-falling hydrometeors are collected most efficiently."

L236: “enhanced are reduced” should read “enhanced or reduced”

Corrected

2 Reviewer #2

The manuscript investigates the aerodynamic impact of the particles’ fall speed measured by a Multi-Angle Snowflake Camera (MASC) using field measurements and Computational Fluid Dynamics (CFD) simulations. It compares the fall speed PDF measured by the MASC and the K-band radar located at the same site. The distribution of fall speed differs from the two instruments and the numerical simulations suggested that the fall speed measured in strong winds ($>$ 5 m/s) would record slower falling particles when not shielded. Similar results were found using the simulations. Overall, this study helps to improve the quality control procedure of the MASC data and contributes significantly to the field of snowfall measurement. It fits well in this journal as it improves the methodology to be used to quality control MASC data. The manuscript is very well written and clear. The figures are also clear and well described in the caption. I have, however, a few main and minor comments should be considered before publication.

Main comments

1. The manuscript gives the impression that the main point is the CFD simulations where it would have been used to study the collection efficiency or to develop transfer function to adjust the MASC measurements. After reading the manuscript, the CFD simulations are used only to explain the field measurements. Given that, I think that the authors should add a methodology section after the introduction that explains the approach taken in this study, which includes the field measurements and the simulations. It may also be useful to present the measurements before showing the results from the simulations.

We agree and have decided to present observations first in addition to changing the title to “Arctic observations and numerical simulations of surface wind effects on Multi-Angle Snowflake Camera measurements” to make it more clear that simulations are supporting the observations and not the other way around.

2. More details should be given about the simulations conducted such as, for example, the number and shape of the mesh used.

We have modified the description as follows:

“The *snappyHexMesh* tool requires an existing base mesh to work with, which is generated from *blockMesh* and is represented in Table 2. For *snappyHexMesh*, two of the most important parameters are *nCellsBetweenLevels*, set to 3, and the *refinementSurfaces* level, which is set to a minimum of 4 and maximum of 5. This brings the total number of cells to 131,864 when the block is $4\ \mathrm{m} \times 4\ \mathrm{m} \times 5\ \mathrm{m}$. These values were determined through analysis of grid independence. For *blockMesh*, the resolution of $25\ \mathrm{cm} \times 25\ \mathrm{cm} \times 25\ \mathrm{cm}$ provided the most efficient mesh for a fixed *snappyHexMesh*. The *snappyHexMesh* parameters were also determined through testing; lower values (e.g., *nCellsBetweenLevels* < 3 or *refinementSurfaces* level < 4)

rendered the mesh too coarse to capture the interaction between particles and flow inside of the aperture, while larger values come at a much higher computational cost."

Did you use the integrated trajectory simulations or developed one?

We have clarified by adding the following sentence to the description of CFD simulations:

"The integrated, semi-developed *solidParticleFoam* is used to simulate particle trajectories, with gravity included to supplement the developed simulation."

Could you add a figure that includes examples of particles' trajectories?

We have added this to the CFD simulations section (Fig. 12 in the revised manuscript)

In Table 2, only one size of particle was used. For dry snow and aggregates, the fall speed does not change much with diameter according to Rasmussen et al. (1999). However, the fall speed of rimed particles can vary a lot with sizes. Why not use more particles' sizes? What would be the impact on your results? Why did you choose a diameter of 2 mm and not 1 mm?

We have added the following to the conclusions section:

"Relatively simple simulations were carried out here to support the findings of the observations analyses. We used only a single set of particles with limited, yet representative characteristics to support observations analyses with simulated particle responses to MASC-perturbed flow. Future work could include a much more diverse set of particle shapes, sizes, and densities, as well as a turbulent dispersion model and other forces that have been neglected in this work."

Please also describe in more details the simulations. For example, is there an updraft as found in previous studies (ex: Colli et al. 2016a,b; Theriault et al. 2012) for the Geonor (shielded and not)? How do you explain that slower falling snowflakes fall is detected by the MASC in stronger winds? Add any other details that could help better understanding the results from the simulations.

We have modified and added the following statements to the CFD simulations text describing the simulated flow perturbed by the MASC as shown in Fig. 2 (which is now Fig. 13 in the revised manuscript):

"There is a clear separation of flow at the upstream side of the aperture, a relatively large upward component above the aperture at the upstream side, and a smaller downward component within the aperture. The fall speeds of particles carried into the aperture by the prevailing flow are decreased by this upward component of the flow, which increases with increasing wind speeds."

3. The simulation as well as the measurement shows that an unshielded MASC leads to a decrease of the fall speed. Can you add a brief explanation in the manuscript? It seems counter-intuitive as faster falling particles would tend to fall in the gauge in stronger winds.

In addition to the above statements added to the CFD simulations section, we have also added the following sentence to the conclusions:

"The simulations revealed that an upward component of perturbed flow at the upstream side of the MASC aperture increases in magnitude with increased wind speed, which in turn leads to a decreased mean particle fall speed."

4. At lower wind speed, larger aggregates tend to be more detected by the MASC than at higher wind speeds. In theory larger ones would fall faster and would not be deflected. How do you explain this finding? Could it be because larger aggregates in strong winds would breakup? Or is it common to report large aggregates in windy conditions at that site? Did you compare with the climatology of solid precipitation at that location?

We have added the following to the discussion section (note that Figs. 8 & 6 and Table 1 correspond to Figs. 12 & 10 and Table 3 in the original manuscript, respectively):

“Larger aggregates with negligible riming tend to be more susceptible than smaller, more dense particles to disturbance by surface winds and associated turbulence, with a tendency for more vertical orientations (Fig. 8), slower fall speeds (Fig. 6), and with a lower frequency of occurrence at higher wind speeds (Table 1) than for other riming classes. The Stokes number is defined as the dimensionless ratio of the particle relaxation time to its terminal velocity in still air v_t/g, and a characteristic time of isotropic, homogeneous turbulent flow. Snowflakes with low Stokes numbers tend to follow the flow, becoming trapped in the vortices with the orientation aligning with the local velocity gradient (Voth & Soldati, 2017). The implication is that large, low-density, aggregate-type hydrometeors — with relatively small values of v_t compared to more heavily rimed particles — have low values of the Stokes number and are more likely to follow the motions of any turbulent flow induced by the MASC aperture. This finding is consistent with prior work by Thériault et al. (2012) who showed that for a Geonor gauge inside a single Alter shield, higher-density, faster-falling hydrometeors are collected most efficiently."

Voth, G. A., & Soldati, A. (2017). Anisotropic particles in turbulence. Annual Review of Fluid Mechanics, 49, 249-276. https://doi.org/10.1146/annurev-fluid-010816-060135

Some minor comments:

1. Lines 5-7: This sentence mentions that the simulations are compared with observations. However, I understood that in this study that the catch efficiency of the instruments is not computed from the simulations and compared with the measured one. But the simulations are used to explain the decrease in fall speed measured in strong winds. This is related to major comment #1. It should be rephrased for clarity.

This has been reworded to state, “Here we present an analysis of Arctic field observations — with and without a Belfort double Alter shield — and compare the results to computational fluid dynamics (CFD) simulations of the airflow and corresponding particle trajectories around the unshielded MASC.”

2. Lines 45: Newman et al. (2009) also conducted CFD simulations in the vicinity of a snowflake video imager. Should probably add the paper to this paragraph. Newman, A. J., P. A. Kucera, and L. F. Bliven, 2009: Presenting the Snowflake Video Imager (SVI). J. Atmos. Oceanic Technol., 26, 167–179, https://doi.org/10.1175/2008JTECHA1148.1.

Added to the end of that paragraph: “CFD simulations were also analyzed for wind flow along the optical axis of a snowflake video imager, with eddies dissipating approximately 1 m downstream of the camera housing and only minor modifications to the wind field (Newman et al., 2009).”

3. Figures 7, 9, 11 and 13: Those figures compare data taken with an unshielded and a shielded MASC. Please clarify in the caption that the shielded and unshielded data were collected during two different periods.

Added to each of those figures' captions: "Unshielded and shielded MASC observations are from two separate periods: 29 November 2015 to 21 August 2016 and 22 August 2016 to 28 August 2018, respectively."

4. Lines 185: Usfc is defined. Could you explain it further and how it compares with standard measurements of wind speed at the instrument's height (or at 10 m)? I may have missed the explanation in the text.

We added the following clarifying sentence to the methods section: "The wind measurement is taken at a standard height of 10 m, which is estimated to be 5(9) m higher than the unshielded(shielded) MASC shown in Fig. 1(2)," where Figs. 1 & 2 correspond to Figs. 5 & 6 in the original manuscript.

5. Lines 189-194: The authors forgot to introduce figure 10. Only Figure 10c is referred to.

We have modified this sentence that begins on line 192 in the original manuscript: "When separated by riming class (Fig. 6), shielded MASC fall speed distributions show discernible differences only for the lightest winds," where Fig. 6 corresponds to Fig. 10 in the original manuscript.

6. Lines 200-201: Please clarify that sentence. I don't understand what you mean by 'more vertical'?

We have clarified the meaning in the sentence as follows:

"…shielded MASC orientation angles tend to be larger for sparsely-rimed aggregates (Fig. 8), meaning their major axes are more often oriented further away from the horizontal plane."

7. Lines 224-229: For clarity, the authors could remind the reader that larger aggregates fall slower than the rimed particles as in Figure 10. We have modified the sentence as follows:

"Larger aggregates with negligible riming tend to be more susceptible than smaller, more dense particles to disturbance by surface winds and associated turbulence, with a tendency for more vertical orientations (Fig. 8), slower fall speeds (Fig. 6), and with a lower frequency of occurrence at higher wind speeds (Table 1) than for other riming classes."

Where Figs. 6 & 8 and Table 1 correspond to Figs. 10 & 12 and Table 3 in the original manuscript, respectively.

3 Reviewer #3

This manuscript summarizes work focused on snow particle observations from a MASC deployed at the NSA site. Specifically, the authors investigate the impact of wind shielding on the MASC instrumentation both from field measurements and from Computational Fluid Dynamics (CFD) simulations. The authors find that the fall speeds from the MASC agreed much better with Doppler velocities from a co-located KAZR for the wind shielded events. Additionally, the CFD simulations indicated slower particle fall speeds when the MASC was unshielded. In general, I think this work is novel and advances the field of in situ snow particle observations. I would also like to commend the authors on an exceptionally well-written manuscript, which had a clear narrative and was enjoyable to read.

I have one major comment and a few minor that should be addressed prior to publication:

Major Comment:

It is unclear to me how many distinct events were used to comprise the observations that were presented. In the methods, the timelines of the MASC deployment unshielded (Feb 2015 – Aug 2016) and shielded (Aug 2016 – Aug 2018)

are outlined (33 months total), however it is not discussed anywhere how many independent events are used in this work. This is key information that is missing from this manuscript as it lends weight to the differences seen between unshielded and shielded observations. This is especially true for Table 3 – as the observations are further divided into wind speed bins and by particle type. A single event could produce 1000s of particle images, so it should be made clear how many independent events were used. This should be added to the methods section – ideally as a table (dates, times). Currently, the manuscript reads as if there are enough observations to say that these fractions of different particle types (in Table 3) are due primarily to the wind shielding impacts, however if there is a low number of independent events (or a low number in a represented wind speed range), then some of these particle type ratios could be from different synoptic or thermodynamic forcing. In addition to including the number of events, the authors should also examine the statistical significance of these differences in particle type (rimed, MR, agg.) for the various wind speed bins (if the N of individual events is large enough).

If only a few independent events were used in this work, I think this should be made clear and the language should reflect that is the case. The implication in the paper (whether purposeful or unconscious) is that the differences in particle type ratios seen in shielded versus unshielded at various wind speeds are a product purely from mitigating the wind to the MASC. However, if very few independent snow events were used in these comparisons the synoptic and thermodynamic conditions could be influencing the ratios of rimed, MR, and aggregate particles.

We have added a paragraph (rather than a table as suggested due to the large number of events) to Section 3.1 (Hydrometeor observations – methods):

“A total of 158,057 particles from 266 distinct events are included here for analysis, with 51 events from the unshielded period of 29 November 2015 to 21 August 2016, and 215 events from the shielded period of 22 August 2016 to 28 August 2018. Distinct events were identified by a length of time between MASC precipitation measurements of $>$ 12 hours, or by a length of time of $>$ 3 hours with an accompanying change of pressure of at least 2 mb. These thresholds were determined by analyzing the period of 4 to 17 December 2017, during which 14,528 precipitation particles were associated with five distinct events as determined by manual inspection of the KAZR reflectivity time series (not shown). Differences in riming class composition for various wind speed categories are determined to be statistically significant by comparing χ distributions using the two-sample Kolmogorov-Smirnov Test at a 5% significance level. In each test, one sample is from the high-wind category ($U_{sfc} > 5\,\mathrm{m\,s^{-1}}$) and the other is from the respective low-wind category.”

The number of distinct events for each case in Table 3 (which is now Table 1 in the revised manuscript) has been added as a whole number in parentheses, and statistical significance is indicated with * (for wind-shielded cases only).

Minor Comments:

Figure 2 illustrates a CFD simulation across the MASC in the +y direction, which is roughly parallel to the cameras that protrude above the opening. And Fig. 3 shows the impact of the fall speeds for ambient winds in both +y and –x (which I read to be winds toward the cameras). What is the impact of the winds originating from behind the cameras, as this is a large obstacle adjacent to the observing ring? I assume that this direction (+x) will have a larger impact

on the particle fall speeds (if I am reading the orientation of the axes correctly). Did you do simulations with the wind originating from behind the cameras?

We added the following sentence towards the end of the CFD Simulations section:

"Although there is little difference between the wind directions shown in Fig. 14, particles carried by flow in the $+x$ direction were mostly blocked by the LEDs located on top of the MASC, especially for speeds of $> 2\,\mathrm{m\,s^{-1}}$ (not shown)."

Along those same lines, wind direction impacts were noted in the discussion about the simulations (minimal), but not in the observations. Was there any analysis on the impacts of wind direction from the observational perspective?

Only a limited amount of wind direction analysis was performed to understand prevailing wind directions. However, we feel that a proper analysis could not be performed for this site without a better understanding of the precision of MASC alignment and how the wind direction changes between the 10-m wind measurement height and the MASC height ($\sim$5 m when unshielded, $\sim$1 m when shielded). Furthermore, the LEDs on top of the MASC affect a relatively limited range of wind directions, and actual particle trajectories are much more complicated than our simulations, making wind direction analysis much more complicated than that of wind speed.

The MASC fall speeds were compared to the KAZR Doppler velocities, and it seems that the mean Doppler velocity from the cloud base to near-surface (I assume) profile was used – is that correct? If so, what was the lowest near-surface bin used in the Doppler velocity profile mean calculation (assuming near-surface to cloud base mean value)? Also, the snow particles can change between the cloud base and the surface – so what is the advantage of using the mean DV value of the profile (near-surface to CB) versus simply using the near-surface Doppler velocity? My instinct is that using the near-surface Doppler velocity value would give you a more direct comparison to the MASC

The intent in using the mean value for all height bins below cloud base was to average out any errors that might be prone to any one height bin. In any case, a comparison of results using the lowest bin vs. all bins below cloud base revealed no substantial differences in the KAZR mean Doppler velocities.

~~Numerical simulations and~~ Arctic observations and numerical simulations of surface wind effects on Multi-Angle Snowflake Camera measurements

Kyle E. Fitch[1,2], Chaoxun Hang[3,4], Ahmad Talaei[1], and Timothy J. Garrett[1]

[1]Department of Atmospheric Sciences, University of Utah, Salt Lake City, 84112, USA
[2]Department of Engineering Physics, Air Force Institute of Technology, Wright-Patterson Air Force Base, Ohio, 45433, USA
[3]Department of Civil Engineering, Monash University, Clayton, 3168, Australia
[4]School of Oceanography, Shanghai Jiao Tong University, Shanghai, 200240, China

Correspondence: Kyle Fitch (kyle.fitch@afit.edu)

Abstract.

Ground-based measurements of frozen precipitation are heavily influenced by interactions of surface winds with gauge-shield geometry. The Multi-Angle Snowflake Camera (MASC), which photographs hydrometeors in free-fall from three different angles while simultaneously measuring their fall speed, has been used in the field at multiple mid-latitude and polar locations both with and without wind shielding. Here we ~~show results of~~ present an analysis of Arctic field observations — with and without a Belfort double Alter shield — and compare the results to computational fluid dynamics (CFD) simulations of the airflow and corresponding particle trajectories around the unshielded MASC~~and compare these results to Arctic field observations with and without a Belfort double Alter shield. Simulations in the absence of a wind shield show a separation of flow at the upstream side of the instrument, with an upward velocity component just above the aperture, which decreases the mean particle fall speed by 55%(74%) for a wind speed of $5\,\mathrm{m\,s^{-1}}$($10\,\mathrm{m\,s^{-1}}$).~~. MASC-measured fall speeds compare well with Ka-band Atmospheric Radiation Measurement (ARM) Zenith Radar (KAZR) mean Doppler velocities only when winds are light ($\leq 5\,\mathrm{m\,s^{-1}}$) and the MASC is shielded. MASC-measured fall speeds that do not match KAZR measured velocities tend to fall below a threshold value that increases approximately linearly with wind speed but is generally $< 0.5\,\mathrm{m\,s^{-1}}$. For those events with wind speeds $\leq 1.5\,\mathrm{m\,s^{-1}}$, hydrometeors fall with an orientation angle mode of 12° from the horizontal plane, and large, low-density aggregates are as much as five times more likely to be observed. Simulations in the absence of a wind shield show a separation of flow at the upstream side of the instrument, with an upward velocity component just above the aperture, which decreases the mean particle fall speed by 55% (74%) for a wind speed of $5\,\mathrm{m\,s^{-1}}$ ($10\,\mathrm{m\,s^{-1}}$). We conclude that accurate MASC observations of the microphysical, orientation, and fall speed characteristics of snow particles require shielding by a double wind fence and restriction of analysis to events where winds are light (~~$\leq 5\,\mathrm{m\,s^{-1}}$~~$\leq 5\,\mathrm{m\,s^{-1}}$). Hydrometeors do not generally fall in still air, so adjustments to these properties' distributions within natural turbulence remain to be determined.

1 Introduction

Accurate measurement of snowfall is of importance to a wide range of scientific and public interests, including weather and climate prediction and monitoring (Yang et al., 2005; Rasmussen et al., 2012; Thériault et al., 2015; Mekis et al., 2018), hydrological cycles (Yang et al., 2005; Rasmussen et al., 2012; Thériault et al., 2012; Mekis et al., 2018), ecosystem research (Rasmussen et al., 2012), snowpack monitoring and disaster management (Thériault et al., 2015; Mekis et al., 2018), transportation (Rasmussen et al., 2001; Thériault et al., 2012, 2015), agriculture (Mekis et al., 2018), and resource management (Thériault et al., 2015; Mekis et al., 2018).

A persistent limitation of these studies is that catch-style precipitation gauges are prone to large uncertainties, especially when measuring snowfall in high winds ~~–~~ — a bias referred to as “under-catch" (Groisman et al., 1991; Groisman and Legates, 1994; Goodison et al., 1998; Rasmussen et al., 2001; Yang et al., 2005). A common remedy is to apply a correction based primarily on wind speed (Yang et al., 1993; Rasmussen et al., 2001, 2012; Wolff et al., 2015), although hydrometeor type (Thériault et al., 2012) and a dynamic drag coefficient (Colli et al., 2015) may also be considered. The correction is calculated by measuring the collection efficiency for a particular gauge or gauge-shield geometry, where collection efficiency is defined as the ratio of the gauge-measured precipitation rate to the best-estimate rate (Thériault et al., 2012). The Double Fence Intercomparison Reference (DFIR) is the standard reference, as determined by the World Meteorological Organization (WMO; Goodison et al., 1998); however, the DFIR has its own uncertainties which can lead to underestimation (Yang et al., 1993) or even overestimation (Thériault et al., 2015) of snowfall rates.

Surface-based measurements of solid precipitation fall speed (Garrett and Yuter, 2014), fall orientation (Garrett et al., 2015; Jiang et al., 2019), and size distributions (Thériault et al., 2012) are all very sensitive to wind speed, with fall speed and size distribution having a strong influence on precipitation gauge collection efficiency (Thériault et al., 2012, 2015). Accurate measurement of solid precipitation characteristics is important for constraining the densities and size distributions used in bulk microphysical parameterizations (e.g., Thompson et al., 2008; Morrison and Milbrandt, 2015). These parameters strongly influence bulk fall speed, highlighted by the Intergovernmental Panel on Climate Change (IPCC) as a critical factor for determining climate sensitivity (Flato et al., 2013). Likewise, knowledge of preferential hydrometeor orientation angles leads to the improved inference of hydrometeor shapes from backscattered polarimetric radar intensities (Vivekanandan et al., 1991, 1994; Matrosov et al., 2005; Matrosov, 2015), and these shapes combine with density to determine hydrometeor fall speeds (Böhm, 1989).

Past studies have typically combined airflow modeling and field observations to ~~understand better~~ better understand the measurement error induced by winds and gauge geometry. Computational fluid dynamics (CFD) calculations are used to characterize the wind velocity field and its interaction with various stationary objects in turbulent flows (Moat et al., 2006; Dehbi, 2008; Ferrari et al., 2017). Thériault et al. (2012) combined field observations and CFD simulations to better understand the scatter in collection efficiency as a function of wind speed for a Geonor, Inc. precipitation gauge located in a single Alter shield. Findings suggested that in addition to wind speed, the hydrometeor collection efficiency is a function of both hydrometeor type and size distribution. For example, hydrometeors such as graupel, with a relatively large density-to-surface-area ratio, fall faster and are collected more efficiently than large, low-density, aggregate-type hydrometeors. Additionally, Colli et al. (2016a, b) compared shielded and unshielded gauge configurations using both time-averaged and time-dependent CFD simulations and found that a single Alter shield was effective in reducing the magnitude of turbulent flow above the gauge aperture. However, upwind shield deflector fins still produced turbulence that propagated into the collection area and generally reduced the collection efficiency. CFD simulations were also analyzed for wind flow along the optical axis of a snowflake video imager, with eddies dissipating approximately 1 m downstream of the camera housing, resulting in only minor modifications to the wind field (Newman et al., 2009).

One instrument that has received increased attention, but whose sampling characteristics have yet to be characterized in detail, is the Multi-Angle Snowflake Camera (MASC; Garrett et al., 2012). The MASC system has overall dimensions of 43.5 ~~cm~~ cm x 58 ~~cm~~ cm x 21.5 ~~cm~~ cm (Stuefer and Bailey, 2016) and observes particles falling into a ~~ring-shaped collection area. The ring~~ hollow decagonal-prism-shaped collection volume. The system's casing houses three cameras focused on a point at the ~~ring center~~ center of the collection volume 10 ~~cm~~ cm away, with each camera separated by 36° ~~(Garrett et al., 2012)~~ (for more details, see Fig. 1 from Garrett et al., 2012). A coupled system of directly opposing near-infrared emitters and detectors, vertically separated by 32 mm, ~~detect~~ detects falling hydrometeors larger than ~~approximately~~ $\sim$0.1 mm in maximum dimension (Garrett and Yuter, 2014). This triggers the cameras and three high-powered LEDs located directly above ~~(Garrett and Yuter, 2014)~~on top of the casing. The time between triggers of the upper and lower emitter-detector pairs yields a fall speed. High-resolution images are captured at an exposure time of 1/25,000th of a second, sufficient to capture a vertical resolution of 40 µm in a hydrometeor falling at $1\,\mathrm{m\,s^{-1}}$ (Garrett et al., 2012).

The MASC system has helped to advance precipitation measurement by automating simultaneous high-resolution photography and fall speed measurement of falling hydrometeors from multiple angles, removing the need for tedious manual collection. Variables derived from the high-resolution images include those describing a hydrometeor's size, shape, fall orientation, and approximate riming degree (Garrett et al., 2012; Garrett and Yuter, 2014; Garrett et al., 2015). As these hydrometeor properties are crucial for accurate numerical modeling and microwave scattering calculations, the MASC has been used at various polar and mid-latitude locations to constrain microphysical characteristics ~~(Garrett et al., 2012; Garrett and Yuter, 2014; Garrett et al., 2015; Grazioli~~ (e.g., Grazioli et al., 2017; Dunnavan et al., 2019; Jiang et al., 2019; Vignon et al., 2019), improve radar-based estimates of snowfall rates (Gergely and Garrett, 2016; Cooper et al., 2017; Schirle et al., 2019), automatically classify hydrometeors (Praz et al., 2017; Besic et al., 2018; Hicks and Notaroš, 2019; Leinonen and Berne, 2020; Schaer et al., 2020), reconstruct particle shapes (Notaroš et al., 2016; Kleinkort et al., 2017) and size distributions (Cooper et al., 2017; Huang et al., 2017; Schirle et al., 2019), and as ground truth comparisons for radar measurements (Bringi et al., 2017; Gergely et al., 2017; Matrosov et al., 2017; Kennedy et al., 2018; Oue et al., 2018; Matrosov et al., 2019). Unlike more common precipitation gauges, the wind velocity field in the proximity of the MASC has not been simulated for various surface winds speeds, directions, or turbulence kinetic energies (TKE).

Studies of hydrometeor behaviors using the MASC have shown, somewhat surprisingly, that frozen hydrometeor fall speeds are only weakly dependent on their size or shape, particularly under conditions of high turbulence intensity (Garrett and Yuter, 2014). Prior studies had shown a much stronger dependence but had theoretically assumed or experimentally arranged for falling hydrometeors to settle in still air (Locatelli and Hobbs, 1974; Böhm, 1989). MASC measurements led to a hypothesis that snow "swirls" in turbulent air in a manner that spreads particle fall speeds to both higher and lower values (Garrett and Yuter, 2014) ~~–~~— an effect shown in prior work to be non-negligible in turbulent flows (Nielsen, 2007). While the fact that snowflakes can just as readily move upwards as downwards is easily verified by any casual observations of a winter storm, it has remained unclear the extent to which the measurements of snowflake fall speed obtained by the MASC have been reflective of reality rather than some artifact of interactions of surrounding winds with the instrument body.

In this study, we ~~describe CFD simulations of hydrometeor-instrument interactions with specific application to the MASC. We compare these simulations to~~ analyze field observations of hydrometeor characteristics from a MASC located in the Arctic and compare these results to CFD simulations of hydrometeor-MASC interactions. The goal of this study is to better understand and characterize the influence of ambient wind speeds on MASC measurements of hydrometeor fall speed, fall orientation, ~~and size distribution~~size distribution, and riming degree for both wind-shielded and unshielded configurations.

~~(a) original MASC model as a Stereolithography (STL) file; (b) MASC model neglecting small-scale details (e.g., bolts, holes, patches, etc.); (c)–(e) snapped mesh on MASC in three viewing directions.~~

2 ~~CFD simulations~~

~~To explore how ambient winds affect MASC measurements of fall speed, we use the OpenFOAM 4.1 tool (Jasak et al., 2007) for CFD calculations of falling particles and winds interacting with the MASC body. OpenFOAM is an open-source CFD toolbox based on C++ libraries and codes designed to solve complex flow dynamics problems (Jasak et al., 2007; Chen et al., 2014; Greensh . The solver uses the factorized finite volume method (FVM) with the Semi-Implicit Method for Pressure Linked Equations (SIMPLE) algorithm (Caretto et al., 1973) to solve the Navier–Stokes equations. The~~ ~~k–ω~~ ~~Shear Stress Transport (SST) model is utilized in this study to solve the turbulence closure problem due to its capability to capture the flow separation near objects through the viscous sub-layer, without additional wall functions (Menter, 1993). We combine the incompressible, robust~~ ~~*simpleFOAM*~~ ~~solver for steady incompressible turbulent flows (Balogh et al., 2012; Higuera et al., 2014) with the~~ ~~*solidParticle*~~ ~~and~~ ~~*solidParticleCloud*~~ ~~classes to study the motions of particles (Iudiciani, 2009).~~

~~To study particle-air interactions, the first step is to determine the two-phase flow type. The ratio between the average inter-particle distance and the particle diameter is estimated. Provided the ratio is~~ ~~$\gtrsim$~~ ~~100, the flow can be treated as a dilute dispersed system, and one-way coupling – wherein the particles do not collide with each other and also do not affect the flow field – can be assumed (Elghobashi, 1994). The OpenFOAM~~ ~~*blockMesh*~~ ~~and~~ ~~*snappyHexMesh*~~ ~~tools are applied here to generate a mesh around the complex physical geometry of the MASC instrument (Gisen, 2014). The~~ ~~*snappyHexMesh*~~ ~~utility automatically generates 3D meshes containing hexahedra and split-hexahedra efficiently. Figure 11(c–e) shows the MASC mesh for different viewing angles. Spatial and temporal parameters are provided in Table 2.~~

~~Domain size and fluid and particle properties of simulations~~ ~~**Domain Dimensions**~~ ~~Width (x–dir) 4 Transverse thickness (y–dir)4 Height (z–dir) 10 Grid (x × y × z) 16 × 16 × 40~~ ~~**Particle properties**~~ ~~Number of particles 400 Diameter (D_p) 2 Density (ρ_p) 50~~ ~~**Fluid properties (at 0 °C)**~~ ~~Viscosity (μ) 1.34×10^{-5} Density (ρ_f) 1.284~~

~~For the simulation of hydrometeors in the atmosphere, we track spherical particles of mass m_p, diameter D_p, and area A_p within a Lagrangian framework, where the Eulerian fluid velocity field $\boldsymbol{v}_f = v_{f_x}\hat{x} + v_{f_y}\hat{y} + v_{f_z}\hat{z}$ is interpolated from nearby grid points at the position of the particle to compute the instantaneous particle drag. The particle velocity $\boldsymbol{v}_p$ is calculated at each time step by assuming that the particle's Reynolds number Re_p is greater than unity, which gives a reduced form of the Maxey–Riley equation of motion (Maxey and Riley, 1983):~~

~~$m_p \frac{d\boldsymbol{v}_p}{dt} = m_p\boldsymbol{g} - \frac{1}{2}C_D(Re)\rho_f A_p|\boldsymbol{v}_p(t) - \boldsymbol{v}_f(t)|(\boldsymbol{v}_p(t) - \boldsymbol{v}_f(t))$~~

~~where the drag coefficient $C_D(Re)$ is a function of the relative Reynolds number $Re = \frac{(v_p - v_f)D_p}{\mu}$, ρ_f is the fluid density, and g is the gravitational constant. Particles measured with the MASC had a median Re_p of 108, with 95% of the values in the range of $40 < Re < 360$.~~

~~In simulations of the response of the particles to horizontal winds in the vicinity of the MASC, the particles are evenly distributed on a 20×20 grid with 1 spacing in the x–direction and 2 spacing in the y–direction. The particles fall downward at an initial velocity of $1\,\mathrm{m\,s^{-1}}$ from a height of $3\,\mathrm{m}$ above the MASC in the $-z$ direction under the force of gravity, reaching an average terminal velocity of $1.05\,\mathrm{m\,s^{-1}}$ well before encountering flows perturbed by the MASC.~~

2 Hydrometeor observations

2.1 Methods

Processing of MASC imagery consists of distinguishing foreground pixels from background to define the region of interest (ROI) and then fitting the ROI with a bounding ellipse (Shkurko et al., 2018). The maximum dimension D_{max} is defined as the length of the ellipse's major axis ~~is defined as the maximum dimension D_{max}~~ for each image. The absolute value of the angle between ~~D_{max}~~ the major axis and the local horizontal plane is the orientation angle θ (Garrett et al., 2012; Garrett and Yuter, 2014; Garrett et al., 2015; Shkurko et al., 2018). A complexity parameter χ is used to distinguished riming classes (Garrett and Yuter, 2014). Here we use $\chi \leq 1.35$ to identify heavily rimed graupel, $1.35 < \chi \leq 2.00$ for moderate riming, and $\chi > 2.00$ indicates sparsely-rimed aggregates. We note that a value of 1.75 was used to distinguish moderately rimed particles from aggregates for Utah snow measurements in Garrett and Yuter (2014), with the observation that the value is subjectively determined by visual inspection of hydrometeor images and varies with location. Mean values of fall speed v_p, D_{max}, θ, and χ from all three images are used for each particle.

A MASC was installed at the Department of Energy's Third Atmospheric Radiation Measurement (ARM) Mobile Facility (AMF3), Oliktok Point, Alaska, in February 2015. The initial deployment was atop a group of shipping containers with no wind shield (Fig. 1). On 22 August 2016, the MASC was relocated to ground level and placed inside of a Belfort Model 36001 Double Alter Wind Shield (Fig. 2). The central camera was pointed in the east-northeasterly direction (Jiang et al., 2019), with surface wind observations showing this to be the predominant wind direction for the present study. The inner (outer) fence of the shield is 1.22 (2.44) ~~m~~ m in diameter, with 32 (64) deflector fins that are each 46 (61) ~~cm~~ cm in length. Observations used

~~Simulated wind field around the MASC with undisturbed winds set at $1\,\mathrm{m\,s^{-1}}$ towards the positive y–direction. Color represents the vertical wind speed v_{f_z}, and arrows show wind vectors on the y–z plane. The cross-section is in the middle of the aperture on the y–z plane, and x–positive points out of the page.~~

~~Figure 13 shows interactions of a horizontal flow in the +y direction of 1 with the MASC body. There is a clear separation of flow on the upstream side of the aperture, a relatively large upward component above the aperture, and a smaller downward component within the aperture.~~

~~Mean fall speed of particles v_p as a function of ambient wind speed. Error bars represent the standard deviation of all the particles at each ambient wind speed. x–negative and y–positive represent the wind pointing towards $-x$ and $+y$ directions (see Fig. 11(d)), respectively. Terminal fall speed v_t is included for comparison, and the initial TKE is 1 .~~

~~The response of particles to these perturbations for horizontal winds in both the $-x$ and $+y$ directions is shown in Fig. 14. There is low sensitivity to wind direction, but the mean particle fall speed within the MASC aperture decreases from $1.07(1.04)\,\mathrm{m\,s^{-1}}$ to $0.30(0.26)\,\mathrm{m\,s^{-1}}$ as the ambient wind speed increases from 1 to $10\,\mathrm{m\,s^{-1}}$ (Table 3).~~

~~Mean fall speed v_p of particles versus ambient wind speed for different values of initial TKE. Terminal fall speed v_t is included for comparison.~~

~~The influence of ambient turbulent intensity expressed as $TKE = \frac{1}{2}\left(\overline{v'^{\,2}_{f_x}} + \overline{v'^{\,2}_{f_y}} + \overline{v'^{\,2}_{f_z}}\right)$ was calculated for $TKE = 1, 3,$ and 5 , where the perturbation velocity v'_f is the difference between the instantaneous and average velocities of the atmospheric flow. These TKE values are used as initial conditions in the k–ω closure model, which determines the shear stress, which in turn is used in the momentum budget equation. Figure 15 shows that for a wind speed of $10\,\mathrm{m\,s^{-1}}$, the mean particle fall speed is 24% lower for an initial value of $TKE = 1\,\mathrm{m^2\,s^{-2}}$ than it is for $TKE = 5\,\mathrm{m^2\,s^{-2}}$ (Table 3).~~

~~Mean particle fall speed for various wind directions, wind speeds, and TKE values. The terminal fall speed is 1.05 in all runs. **Ambient wind** **1** $\mathrm{m\,s^{-1}}$ **2** $\mathrm{m\,s^{-1}}$ **5** $\mathrm{m\,s^{-1}}$ **10** $\mathrm{m\,s^{-1}}$ **Wind Direction** x-negative 1.07 0.92 0.47 0.30 y-positive 1.04 0.91 0.47 0.26 **TKE** 1 1.07 0.91 0.47 0.26 3 1.09 0.96 0.52 0.31 5 1.09 0.98 0.54 0.34~~

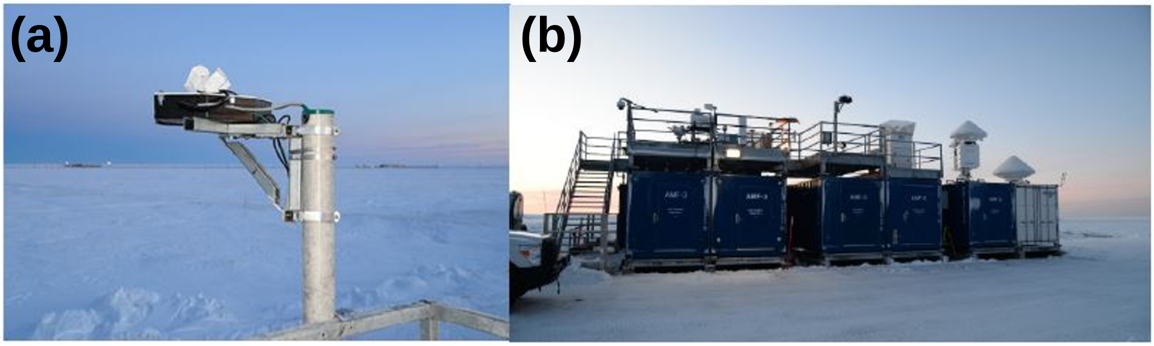

Figure 1. (a) Unshielded MASC configuration at the Third ARM Mobile Facility (AMF3), Oliktok Point, Alaska. (b) Ground-level view of the MASC on top of a group of shipping containers. This was the MASC configuration from initial deployment in February 2015 through 21 August 2016. Image courtesy of the U.S. Department of Energy Atmospheric Radiation Measurement (ARM) user facility.

here include both unshielded and shielded configurations, spanning a 33-month period from 29 November 2015 to 28 August 155 2018 (ARM Climate Research Facility, 2014). Raw data and images were processed with a local University of Utah processing

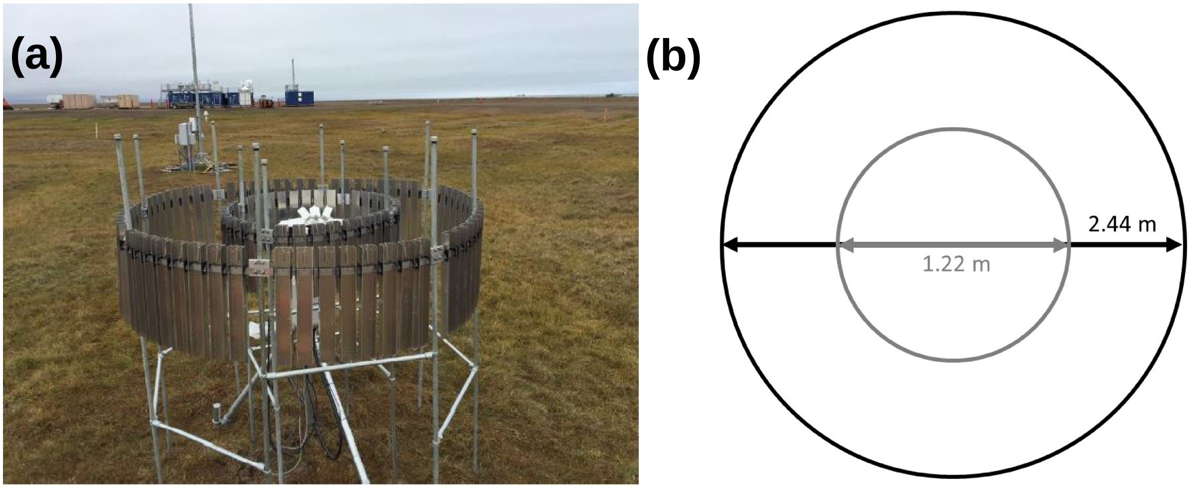

Figure 2. (a) The MASC was relocated to ground level and placed inside a Belfort double Alter shield on 22 August 2016 (field site photograph courtesy of Martin Stuefer). (b) The shield consists of inner and outer fences with diameters of 1.22 m and 2.44 m, respectively.

suite called *mascpy* (The Hive: University of Utah Research Data Repository, 2020a, b), similar to that described in Shkurko et al. (2018).

A total of 158,057 particles from 266 distinct events are included here for analysis, with 51 events from the unshielded period of 29 November 2015 to 21 August 2016, and 215 events from the shielded period of 22 August 2016 to 28 August 2018. Distinct events were identified by a length of time between MASC precipitation measurements of > 12 hours, or by a length of time of > 3 hours with an accompanying change of pressure of at least 2 mb. These thresholds were determined by analyzing the period of 4 to 17 December 2017, during which 14,528 precipitation particles were associated with five distinct events as determined by manual inspection of the KAZR reflectivity time series (not shown). Differences in riming class composition for various wind speed categories are determined to be statistically significant by comparing χ distributions using the two-sample Kolmogorov-Smirnov Test at a 5% significance level. In each test, one sample is from the high-wind category ($U_{sfc} > 5\,\mathrm{m\,s^{-1}}$) and the other is from the respective low-wind category.

To complement MASC observations and characterize the influence of ambient wind speed on MASC measurements, surface wind measurements from a traditional meteorological ground suite (Ritsche, 2011; ARM Climate Research Facility, 2013) were matched to MASC hydrometeors by calculating a mean wind speed U_{sfc} for the 1 minute period leading up to the observation time corresponding to each hydrometeor. The wind measurement is taken at a standard height of 10 m, which is estimated to be 5 (9) m higher than the unshielded (shielded) MASC shown in Fig. 1 (2). In addition to the quality control checks listed in Shkurko et al. (2018), a surface temperature threshold of $< 2\,^\circ\mathrm{C}$ was used to exclude liquid hydrometeors, which are occasionally misidentified by the *mascpy* algorithm.

For a ground truth hydrometeor fall speed, mean Doppler velocity was calculated from the volume of scattering hydrometeors detected by a co-located Ka-band ARM Zenith-pointing Radar (KAZR). At a vertical resolution of 30 ~~m~~m, the KAZR produces measurements of the first three moments of the Doppler spectrum: reflectivity, mean Doppler velocity, and spectrum width (Widener et al., 2012; Oue et al., 2018). The Doppler velocity signal has a resolution of 0.05 $\mathrm{m\,s^{-1}}$ (Oue et al., 2018) and consists of both larger particle fall speeds and the vertical air motions traced by smaller particles (Shupe et al., 2008). Using only Doppler velocity measurements originating from below cloud base, we isolate the signal of the larger, precipitation-sized hydrometeors, while acknowledging the relatively small bias of Doppler broadening from turbulence and wind shear (Shupe et al., 2008). Both mean Doppler velocity and cloud base height were retrieved from the ARM's KAZR Active Remote Sensing of CLouds (ARSCL) Value-Added Product (ARM Climate Research Facility, 2015; Clothiaux et al., 2000).

Results are presented here in the form of probability density function (PDF) estimates, calculated ~~by normalizing the frequency N_i of each histogram bin i of width Δx (equally spaced bins), such that $PDF \simeq \frac{N_i}{N_t \Delta x}$. Here $N_t = \sum N_i$ is the total number of observations, and x is the variable of interest. The resulting PDF estimates were adjusted using a Gaussian kernel smoothing function~~ using a kernel density estimator of the form

$$\hat{f}(x_0) = \frac{1}{n_s h}\sum_{i=1}^{n_s} K\left(\frac{x_0 - x_i}{h}\right) \tag{1}$$

where x_0 is a real value of the distribution being estimated, x_i is a random sample from the distribution, n_s is the sample size, and h is the bandwidth (Wilks, 2011). The Gaussian smoothing function is $K(x) = (2\pi)^{-1/2}\exp(-x^2/2)$ for a random variable x, and h is optimized according to Bowman and Azzalini (1997) to produce a smooth curve. For distributions of D_{max}, the exponential slope parameter λ is computed using a linear least squares regression from the peak of the log-linear distribution through the tail.

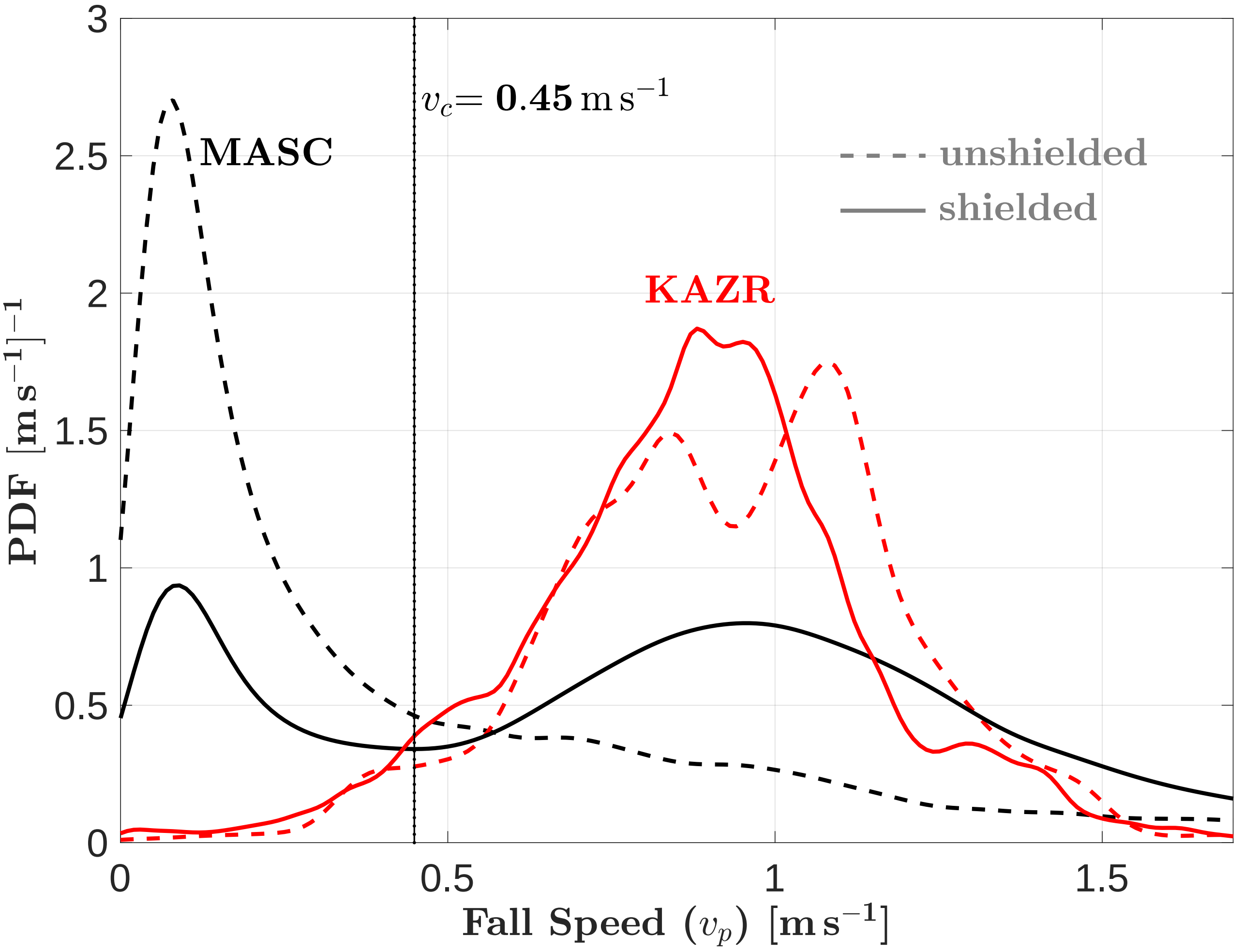

Figure 3. Comparison of fall speed v_p probability density function (PDF) estimates from MASC and KAZR measurements, both with and without wind shielding of the MASC. KAZR fall speeds are determined from the mean Doppler velocity below cloud base (positive downward, see Sect. 2.1 for details). The cutoff fall speed v_c marks the location of the local minimum separating the two modes of the shielded MASC distribution. Unshielded and shielded MASC observations are from two separate periods: 29 November 2015 to 21 August 2016 and 22 August 2016 to 28 August 2018, respectively.

2.2 Observations of fall speed

Distributions of MASC-measured particle fall speed v_p, both with and without a wind shield, are compared to coincident measurements from the KAZR in Fig. 3. The KAZR-measured fall speed mode is $\sim 1\,\mathrm{m\,s^{-1}}$, while the MASC-measured fall speed distribution has a mode of 0.08 $\mathrm{m\,s^{-1}}$ for both the shielded and unshielded cases. However, the shielded MASC fall speed distribution has a second mode at 0.96 $\mathrm{m\,s^{-1}}$, similar to the location of the KAZR mode. Notably, a low-speed mode was not observed in the KAZR measurements despite its velocity resolution of 0.05 $\mathrm{m\,s^{-1}}$.

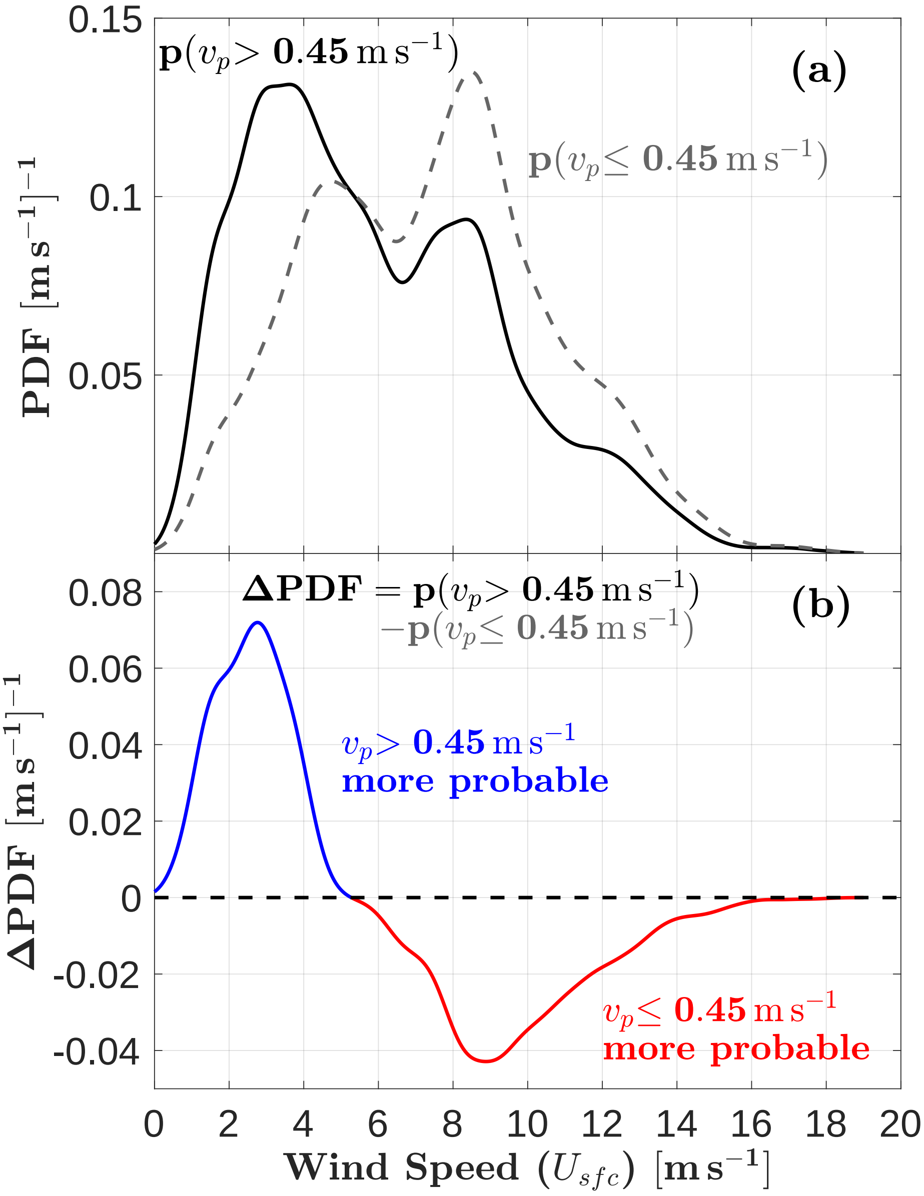

Figure 4. (a) Comparison of, and (b) difference between, estimates of surface wind speed U_{sfc} ~~probability density functions (~~PDFs ~~)~~ for the high ($v_p > 0.45\,\mathrm{m\,s^{-1}}$) and low ($v_p \leq 0.45\,\mathrm{m\,s^{-1}}$) fall speed modes of the shielded MASC fall speed distribution from Fig. 3. $\Delta PDF > 0$ means the probability of $v_p > 0.45\,\mathrm{m\,s^{-1}}$ is greater.

The shielded MASC fall speed distribution deviates substantially from the corresponding KAZR distribution for fall speeds below $0.45\,\mathrm{m\,s^{-1}}$. This is the location of the local minimum separating the two modes of the shielded MASC fall speed distribution and is defined from here on as the cutoff fall speed v_c: the fall speed below which MASC measurements are assumed to be erroneous. The fall speed distribution can therefore be divided into two parts: $v_p > v_c$ and $v_p \leq v_c$.

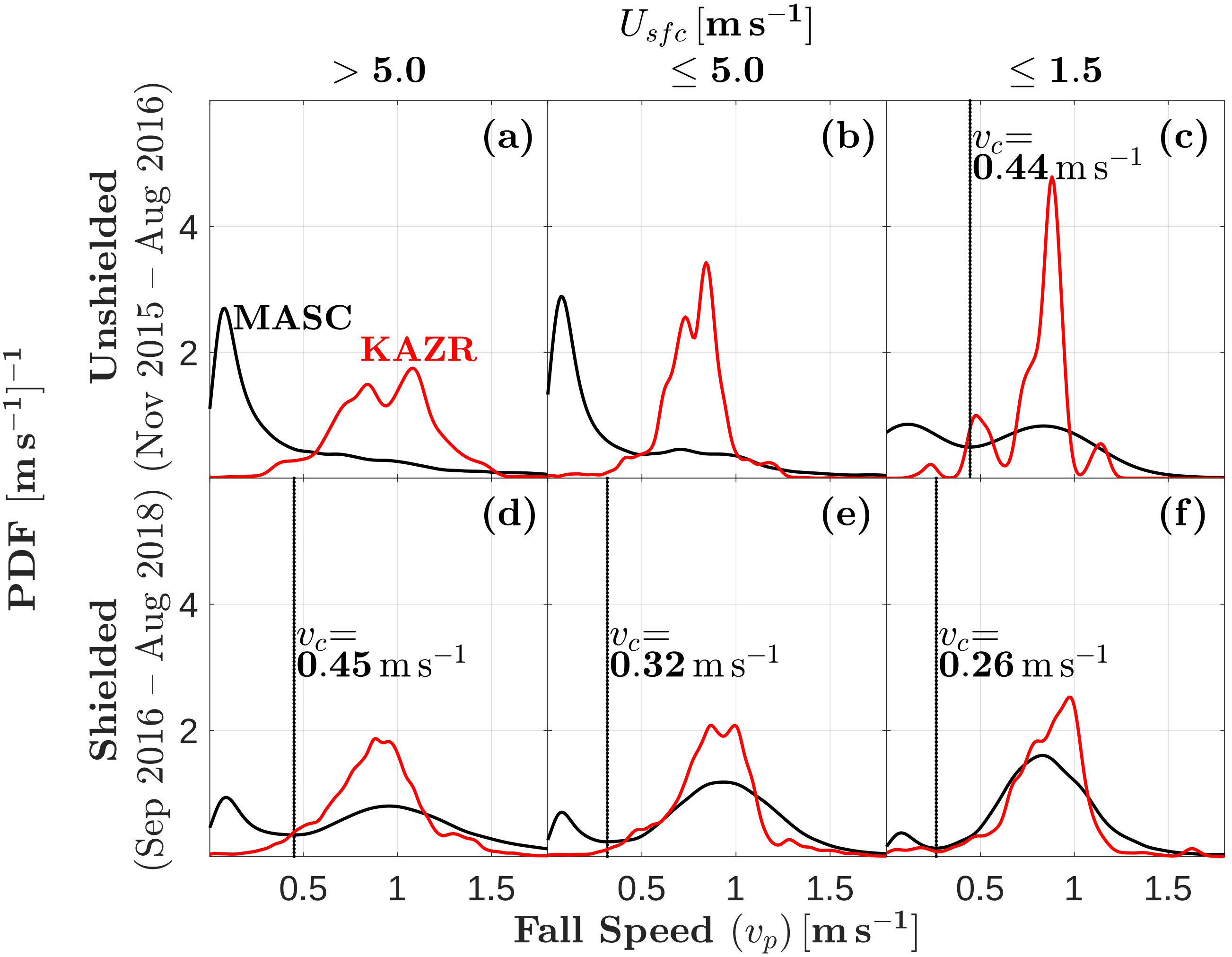

Figure 5. Comparison of MASC hydrometeor fall speed and KAZR mean Doppler fall speed ~~distributions~~ PDF estimates for (a)–(c) unshielded and (d)–(f) shielded MASC measurements. Surface wind speeds U_{sfc} decrease from left to right. Where MASC PDFs are bimodal, the vertical line marks the cutoff fall speed v_c, indicating the location of the local minimum ~~of the PDF~~ separating the two modes. The number of observations for each case is listed in Table 1. The terms "shielded" and "unshielded" refer only to the MASC. Unshielded and shielded MASC observations are from two separate periods: 29 November 2015 to 21 August 2016 and 22 August 2016 to 28 August 2018, respectively.

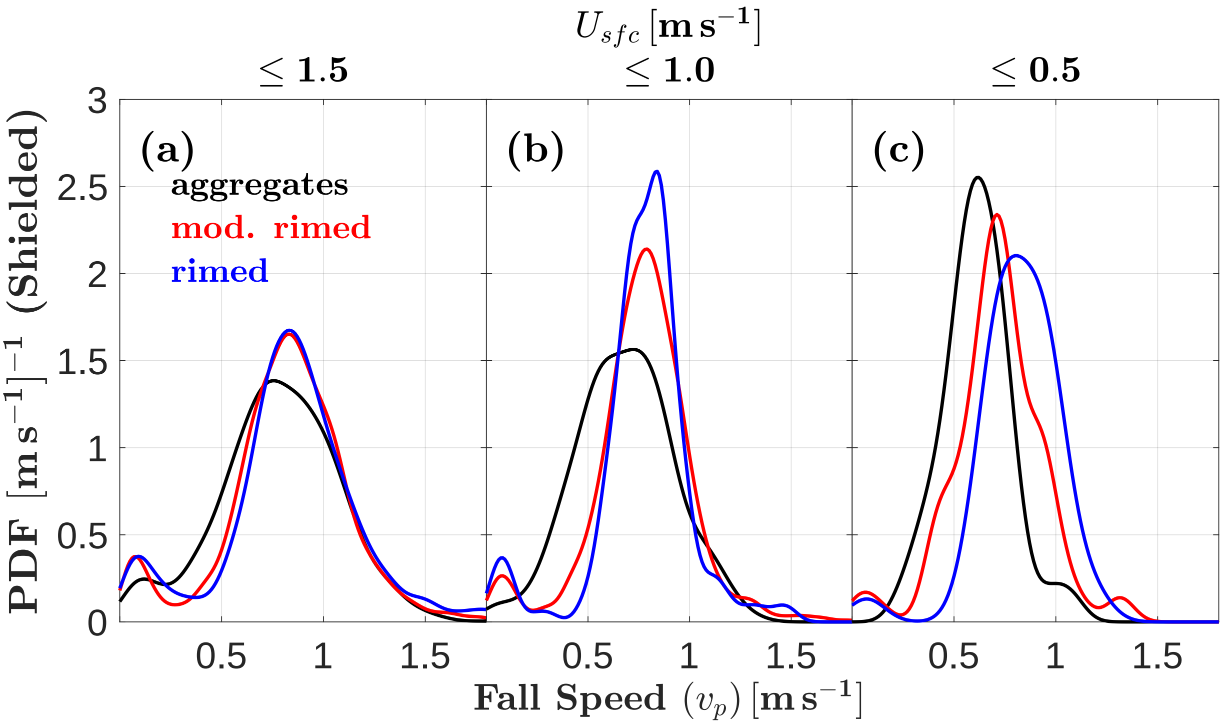

Figure 6. ~~Probability density function (~~PDF ~~)~~ estimates for shielded MASC fall speed v_p for very light wind speeds and hydrometeors divided into three riming classes: sparsely-rimed aggregates, moderately rimed, and rimed.

To examine the influence of surface wind speeds on MASC fall speed measurements, Fig. 4(a) shows PDF estimates of wind speed ~~$U_{sfc} = \sqrt{v_{f_x}^2 + v_{f_y}^2}$~~ U_{sfc} for the two separate parts of the shielded MASC fall speed distribution from Fig. 3. From the difference (Fig. 4(b)), it is apparent that the high-speed mode of $v_p > 0.45\,\mathrm{m\,s^{-1}}$ is more likely to be observed when $U_{sfc} < 5\,\mathrm{m\,s^{-1}}$. ~~This matches well with the simulated fall speeds in wind speeds of $\leq 5\,\mathrm{m\,s^{-1}}$ from Table 3 and Figs. 14 and 15, although the simulation did not include a wind fence.~~

Figure 5 compares MASC and KAZR fall speed distributions as a function of U_{sfc}, again both with and without wind shielding of the MASC. Qualitatively, the agreement between the MASC and KAZR distributions is maximized for shielded MASC measurements with light winds ($U_{sfc} \leq 1.5\,\mathrm{m\,s^{-1}}$), where only 7% of measured fall speeds are lower than the v_c threshold of $0.26\,\mathrm{m\,s^{-1}}$ (Fig. 5(f)). When separated by riming class (Fig. 6), shielded MASC fall speed distributions show discernible differences only for the lightest winds. This is most apparent for $U_{sfc} \leq 0.5\,\mathrm{m\,s^{-1}}$ (Fig. 6(c)), where the most heavily rimed particles ($\chi \leq 1.35$) tend to exhibit the highest fall speeds. Particle counts corresponding to Figs. 5 and 6 are listed in Table 1.

Table 1. Number and percentage of observed hydrometeors in each wind shielding case, surface wind speed U_{sfc} category, and riming class. Whole numbers in parentheses indicate the number of distinct events for each category. For each wind-shielded riming category, * indicates where the difference in the complexity (χ) distribution for each low-wind case is statistically significant at the 5% level from that of the respective high wind case ($U_{sfc} > 5\,\mathrm{m\,s^{-1}}$). Percentages may not add to precisely 100% due to rounding. Less restrictive wind speed categories (e.g., $\leq 5\,\mathrm{m\,s^{-1}}$) include data from more restrictive categories (e.g., $\leq 1.5\,\mathrm{m\,s^{-1}}$).

	U_{sfc}				
Category	$> \mathbf{5}\,\mathrm{m\,s^{-1}}$	$\leq \mathbf{5}\,\mathrm{m\,s^{-1}}$	$\leq \mathbf{1.5}\,\mathrm{m\,s^{-1}}$	$\leq \mathbf{1.0}\,\mathrm{m\,s^{-1}}$	$\leq \mathbf{0.5}\,\mathrm{m\,s^{-1}}$
No Wind Shield	**2,249 (27)**	**5,097 (31)**	**460 (9)**	**167 (7)**	**32 (4)**
Aggregates	176 (8%,16)	1,522 (30%,22)	67 (15%,6)	15 (9%,5)	5 (16%,2)
Moderately Rimed	1,209 (54%,25)	2,891 (57%,27)	315 (68%,8)	115 (69%,6)	14 (44%,4)
Rimed	864 (38%,13)	684 (13%,19)	78 (17%,5)	37 (22%,2)	13 (41%,2)
Wind Shield	**85,151 (181)**	**58,~~939~~939* (140)**	**5,~~730~~730* (45)**	**1,~~372~~372* (30)**	**~~161~~161* (13)**
Aggregates	15,320 (18%,132)	11,304 (19%,101)	1,299 (23%,30)	~~302~~ 302* (22%,21)	~~41~~ 41* (25%,8)
Moderately Rimed	47,147 (55%,165)	35,~~820~~ 820* (61%,128)	3,~~477~~ 477* (61%,38)	~~855~~ 855* (62%,26)	86 (53%,12)
Rimed	22,684 (27%,151)	11,~~815~~ 815* (20%,107)	~~954~~ 954* (17%,35)	~~215~~ 215* (16%,21)	34 (21%,6)

2.3 Observations of orientation, maximum dimension, and riming degree

Distributions of unshielded MASC-measured orientation angles tend to favor high angles in high winds ($U_{sfc} > 5\,\mathrm{m\,s^{-1}}$, Fig. 7(a)), where the mode is 57°, but this shifts to 28° for the lightest winds ($U_{sfc} \leq 1.5\,\mathrm{m\,s^{-1}}$, Fig. 7(c)). Shielded measurements tend towards even lower angles in the lightest winds, with a mode of 12° for $U_{sfc} \leq 1.5\,\mathrm{m\,s^{-1}}$ (Fig. 7(f)). These results suggest that these solid hydrometeors tend to fall with their ~~maximum dimensions~~ major axes nearly aligned with the horizontal plane when left undisturbed by surface winds. When separated by riming class for the lightest winds ($U_{sfc} \leq 1.5\,\mathrm{m\,s^{-1}}$), shielded MASC orientation angles tend to be larger ~~(i.e., more vertical)~~ for sparsely-rimed aggregates (Fig. 8), meaning their major axes are more often oriented further away from the horizontal plane.

To examine surface wind influence on hydrometeor sizes observed by the MASC, distributions of D_{max} and corresponding λ values are shown in Fig. 9. The slope parameter λ is smallest when the MASC is shielded and surface winds are very light ($U_{sfc} \leq 1.5\,\mathrm{m\,s^{-1}}$, Fig. 9(f)), and largest for unshielded observations in high winds ($U_{sfc} > 5\,\mathrm{m\,s^{-1}}$, Fig. 9(a)). This suggests that the largest hydrometeors are less likely to be captured by the MASC in strong winds, and even less likely without shielding. When these wind-shielded distributions are separated into riming degree classes (Fig. 10), aggregates exhibit a 26% percent decrease in λ, from 0.88 to 0.65 $\mathrm{mm^{-1}}$, when comparing the case with high winds ($U_{sfc} > 5\,\mathrm{m\,s^{-1}}$) to that with low winds ($U_{sfc} \leq 1.5\,\mathrm{m\,s^{-1}}$). For a size distribution ~~with the~~ of form $n_{D_{max}} = n_{D_0}\exp(-\lambda D_{max})$, where $n_{D_{max}}\Delta D_{max}$ is the concentration of particles with sizes between D_{max} and $D_{max} + \Delta D_{max}$, this decrease in λ corresponds to a number concentration that is 5 times higher for aggregates with $D_{max} = 7\,\mathrm{mm} \pm \Delta D_{max}/2$. In contrast, moderately and heavily rimed

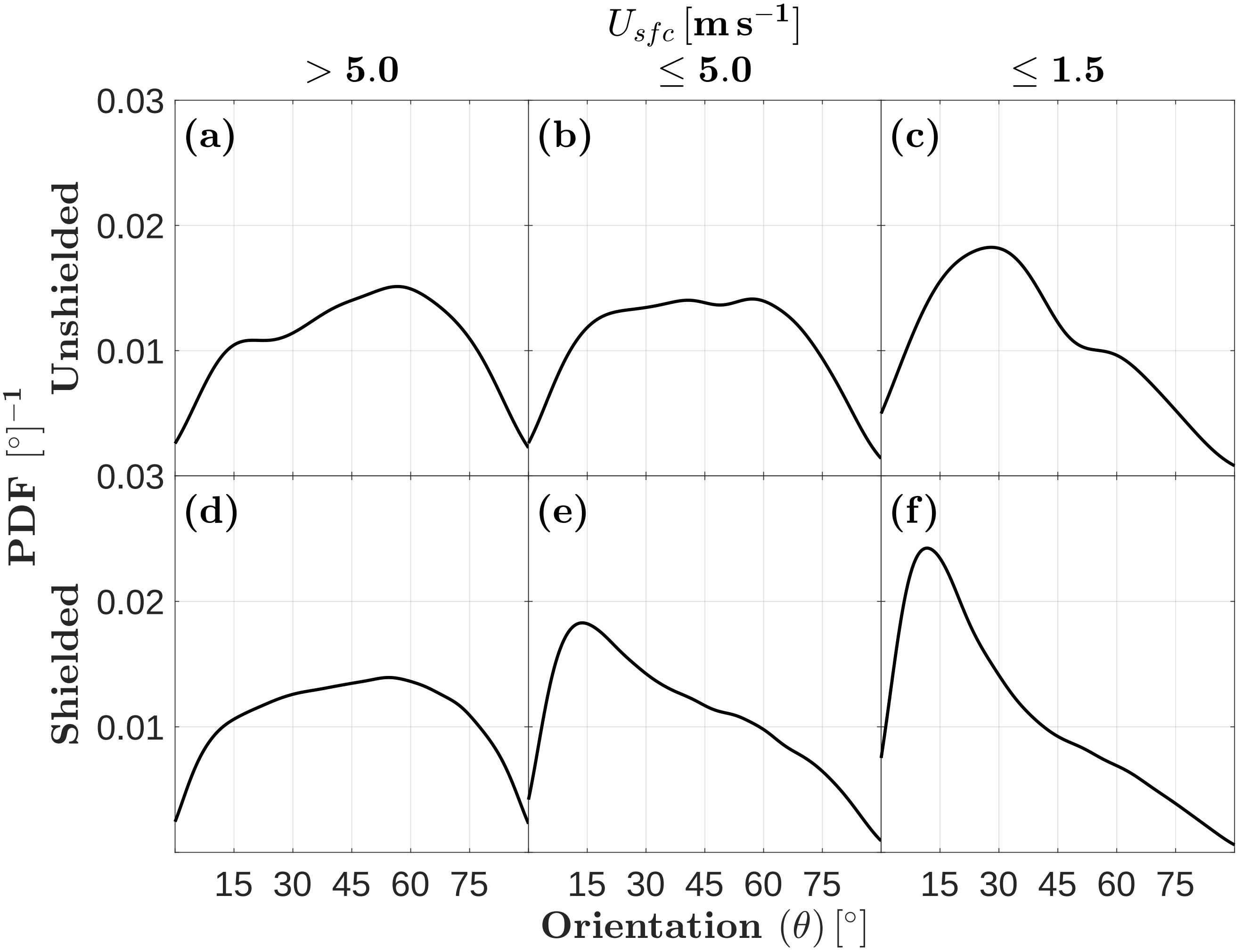

Figure 7. Probability distribution function (PDF) estimates of MASC-observed orientation angle θ as a function of surface wind speed U_{sfc} for both shielded and unshielded configurations. Unshielded and shielded MASC observations are from two separate periods: 29 November 2015 to 21 August 2016 and 22 August 2016 to 28 August 2018, respectively.

hydrometeors only exhibit ~~a~~ decreases in λ ~~decrease~~ of 13% and 11%, respectively, when comparing high- and low-wind measurements.

The observation that measured concentrations of larger aggregates are relatively sensitive to surface winds compared to more heavily rimed particle types suggests that the frequency distribution of riming classes observed by the MASC might also reflect this sensitivity. Indeed, Table 1 shows that the percentage of wind-shielded aggregates reaches a maximum (25%) when wind speeds are lowest ($U_{sfc} \leq 0.5\,\mathrm{m\,s^{-1}}$). The opposite is true for shielded rimed hydrometeors (i.e., graupel), implying that

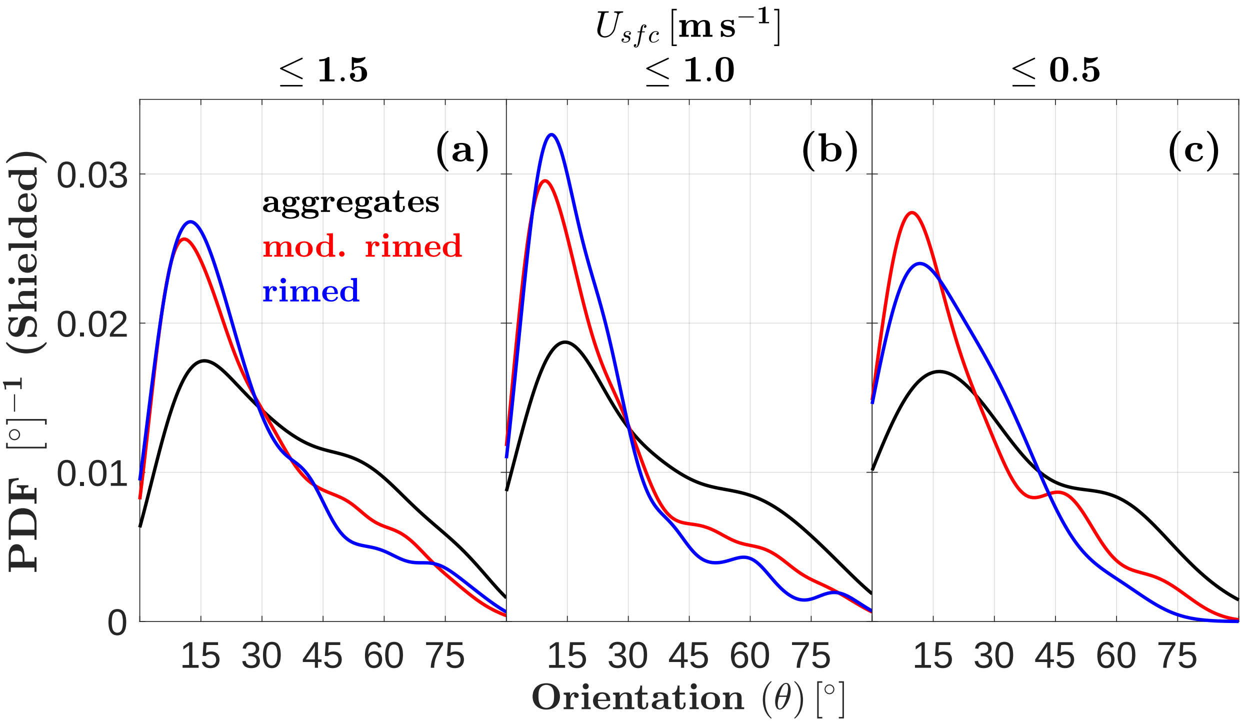

Figure 8. As in Fig. 7 but with lighter winds and hydrometeors divided into three riming degree categories: sparsely-rimed aggregates, moderately rimed, and rimed. Only shielded MASC measurements are shown.

high-density rimed particles are more likely to be observed by the MASC than large, weakly rimed aggregates in the presence of strong winds ($U_{sfc} > 5\,\mathrm{m\,s^{-1}}$).

3 CFD simulations

To explore the fluid-particle-MASC dynamics involved in the influence of ambient winds on MASC measurements of fall speed, we use the OpenFOAM 4.1 tool (Jasak et al., 2007) for CFD calculations of falling particles and winds interacting with the MASC body. OpenFOAM is an open-source CFD toolbox based on C++ libraries and codes designed to solve complex flow dynamics problems (Jasak et al., 2007; Chen et al., 2014; Greenshields, 2015). The incompressible, robust *simpleFoam* solver for steady incompressible turbulent flows (Balogh et al., 2012; Higuera et al., 2014) uses the factorized finite volume method (FVM) with the Semi-Implicit Method for Pressure Linked Equations (SIMPLE) algorithm (Caretto et al., 1973) to solve the Navier–Stokes equations. The k–ω Shear Stress Transport (SST) model is utilized in this study to solve the turbulence closure problem due to its capability to capture the flow separation near objects through the viscous sub-layer, without additional wall functions (Menter, 1993). We combine *simpleFoam* with the *solidParticle* and *solidParticleCloud* classes to study the motions

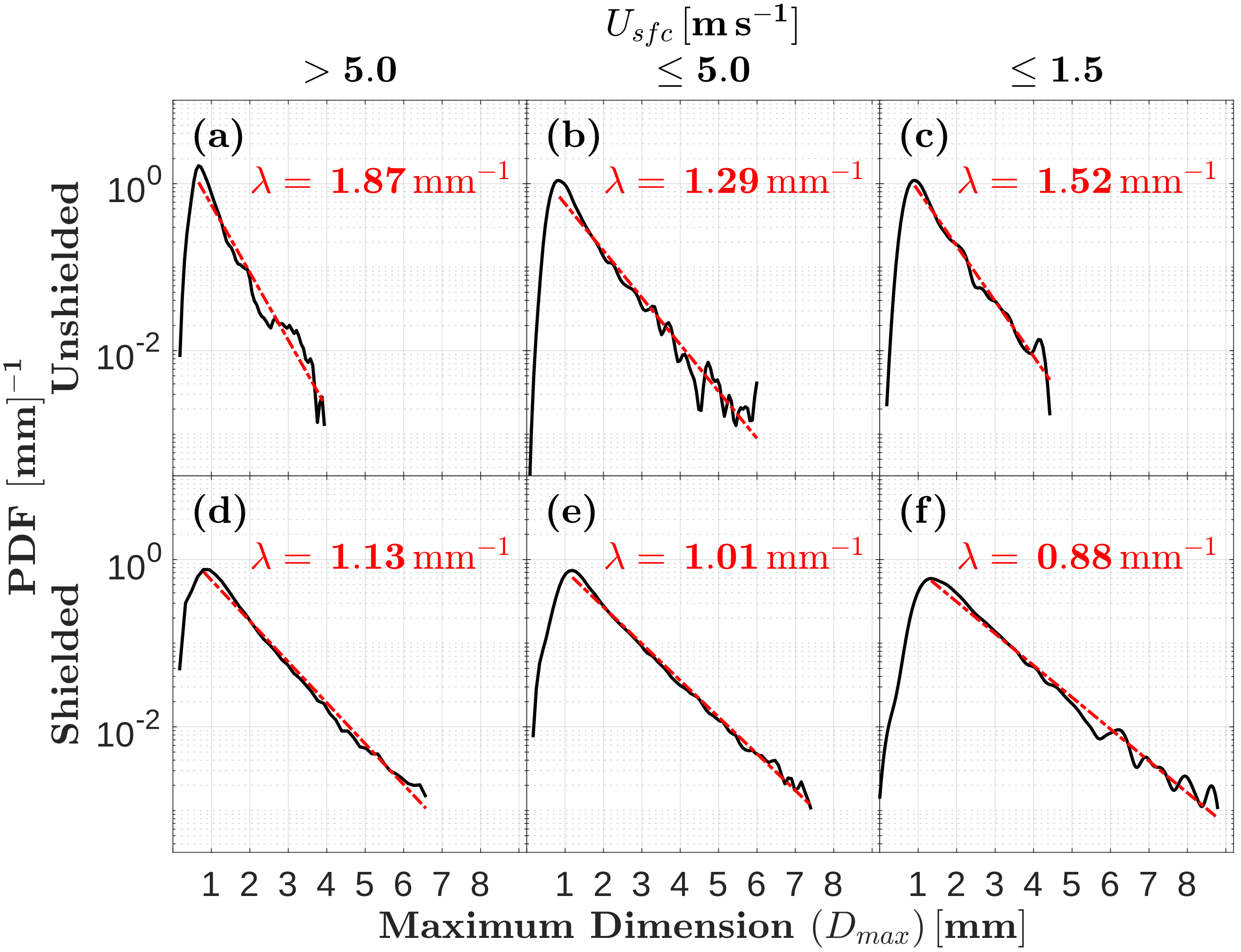

Figure 9. As in Fig. 7 but for maximum dimension D_{max} and slope parameter λ. The slope parameter is calculated as the linear least-squares fit from the peak through the tail of the distribution. Unshielded and shielded MASC observations are from two separate periods: 29 November 2015 to 21 August 2016 and 22 August 2016 to 28 August 2018, respectively.

of particles (Iudiciani, 2009). The integrated, semi-developed *solidParticleFoam* is used to simulate particle trajectories, with gravity included to supplement the developed simulation.

To study particle-air interactions, the first step is to determine the two-phase flow type. The ratio between the average inter-particle distance and the particle diameter is estimated. Provided the ratio is $\gtrsim 100$, the flow can be treated as a dilute, dispersed system, and one-way coupling — wherein the particles do not collide with each other and also do not affect the flow field — can be assumed (Elghobashi, 1994). The OpenFOAM *blockMesh* and *snappyHexMesh* tools are applied here to generate a mesh around the complex physical geometry of the MASC instrument (Gisen, 2014). The *snappyHexMesh* utility

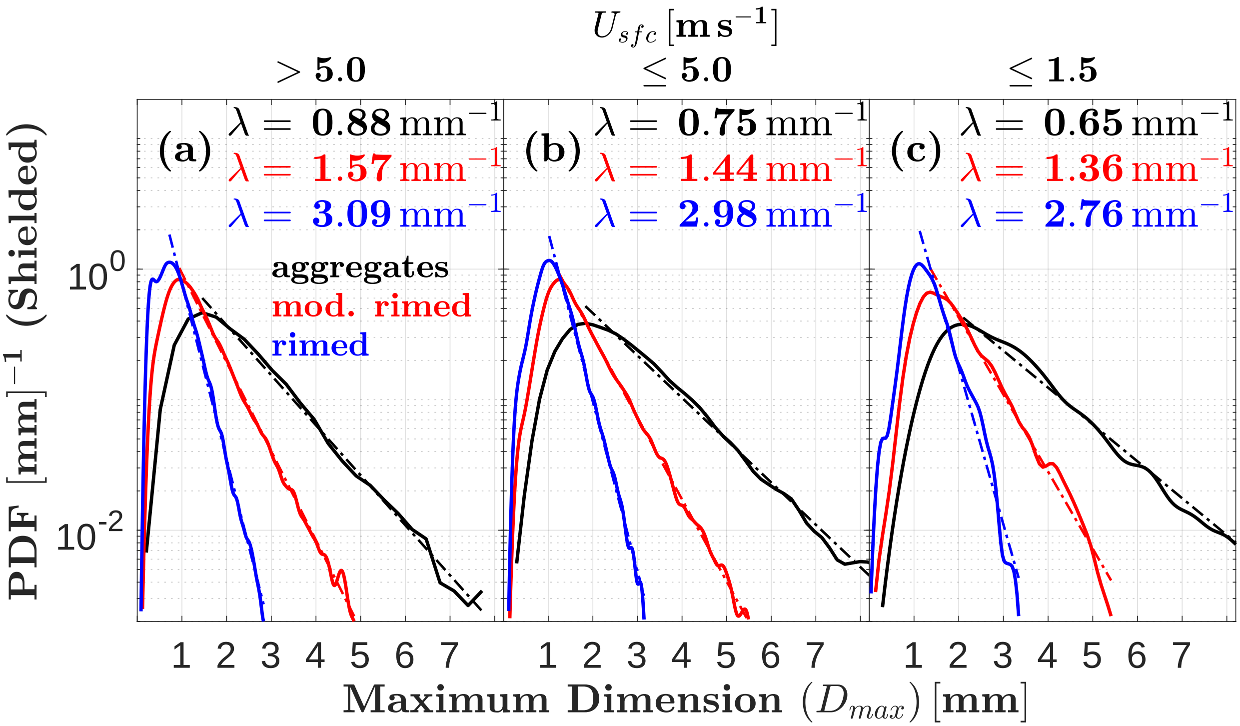

Figure 10. As in Fig. 9 but with hydrometeors divided into three riming degree categories: sparsely-rimed aggregates, moderately rimed, and rimed. Only shielded MASC measurements are shown.

automatically generates 3D meshes containing hexahedra and split-hexahedra from a triangulated surface (MASC in this case). Figure 11(c–e) shows the MASC mesh for different viewing angles. Spatial and temporal parameters are provided in Table 2.

The *snappyHexMesh* tool requires an existing base mesh to work with, which is generated from *blockMesh* and is represented in Table 2. For *snappyHexMesh*, two of the most important parameters are *nCellsBetweenLevels*, set to 3, and the *refinementSurfaces* level, which is set to a minimum of 4 and maximum of 5. This brings the total number of cells to 131,864 when the block is 4 m × 4 m × 5 m. These values were determined through analysis of grid independence. For *blockMesh*, the resolution of 25 cm × 25 cm × 25 cm provided the most efficient mesh for a fixed *snappyHexMesh*. The *snappyHexMesh* parameters were also determined through testing; lower values (e.g., *nCellsBetweenLevels* < 3 or *refinementSurfaces* level < 4) rendered the mesh too coarse to capture the interaction between particles and flow inside of the aperture, while larger values come at a much higher computational cost.

For the simulation of hydrometeors in the atmosphere, we track spherical particles of mass m_p, diameter D_p, and area A_p within a Lagrangian framework, where the Eulerian fluid velocity field $\boldsymbol{v}_f = v_{f_x}\hat{x} + v_{f_y}\hat{y} + v_{f_z}\hat{z}$ is interpolated from nearby grid points at the position of the particle to compute the instantaneous particle drag. The particle velocity $\boldsymbol{v}_p$ is calculated at each time step by assuming that the particle's Reynolds number Re_p is greater than unity, which gives a semi-empirical form

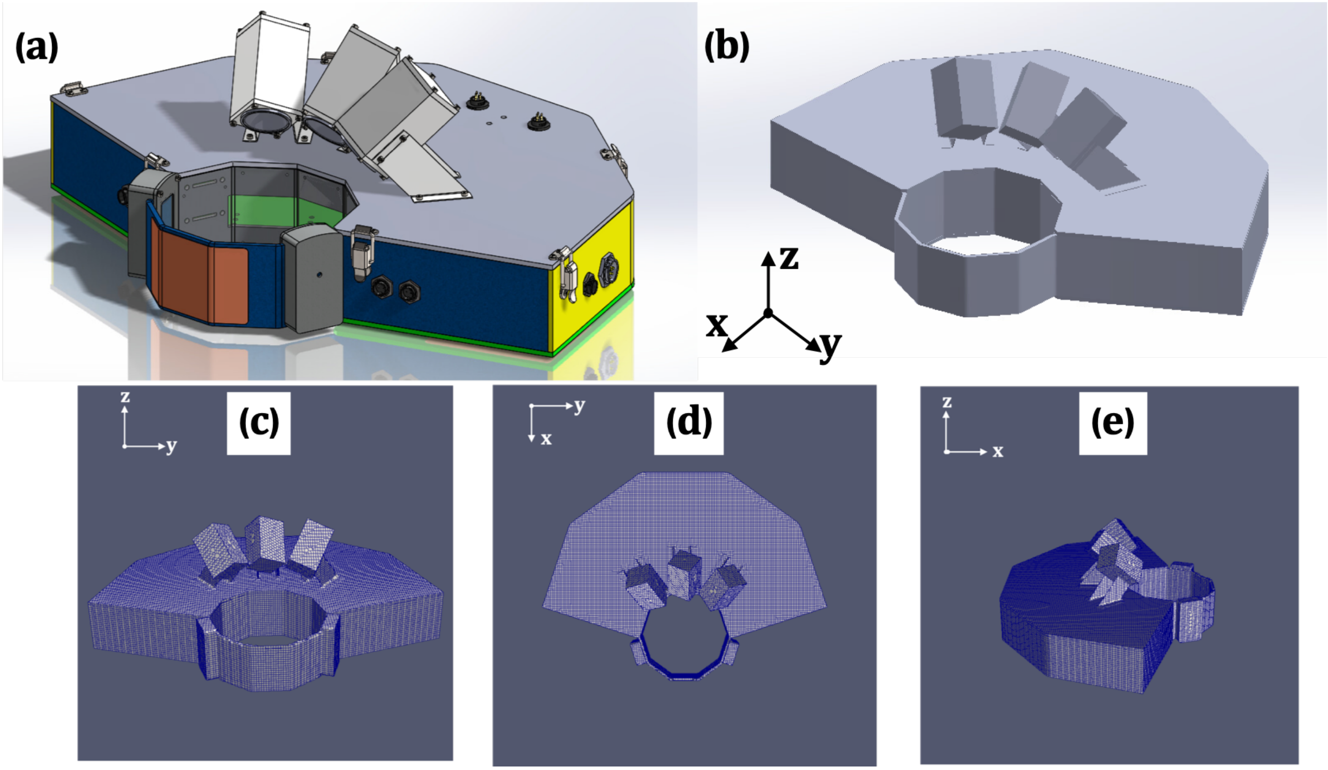

Figure 11. (a) original MASC model as a Stereolithography (STL) file; (b) MASC model neglecting small-scale details (e.g., bolts, holes, patches, etc.); (c)–(e) snapped mesh on MASC in three viewing directions.

of the Maxey–Riley equation of motion (Maxey and Riley, 1983):

$$m_p \frac{d\boldsymbol{v}_p}{dt} = m_p \boldsymbol{g} - \frac{1}{2}\rho_f A_p C_D(Re_p)|\boldsymbol{v}_p(t) - \boldsymbol{v}_f(t)|(\boldsymbol{v}_p(t) - \boldsymbol{v}_f(t)) \tag{2}$$

where the steady drag force F_d changed from scaling linearly with relative velocity to scaling as an empirically derived steady drag coefficient C_D and the relative velocity squared: $F_d = \frac{1}{2}\rho_f A_p C_D(\mathrm{Re_p})(v_p - v_f)^2$. Here ρ_f is the fluid density and g is the gravitational constant. The drag coefficient $C_D(Re_p)$ is defined as

$$C_D = \begin{cases} \frac{24}{Re_p}\left(1 + \frac{1}{6}Re_p^{2/3}\right) & \text{if } Re_p \leq 1000 \\ 0.44 & \text{if } Re_p > 1000 \end{cases} \tag{3}$$

and is a function of the relative Reynolds number $Re_p = (v_p - v_f)D_p/\mu$, where μ is the kinematic viscosity. Particles measured with the MASC had a median Re_p of 108, with 95% of the values in the range of $40 < Re_p < 360$. The boundary conditions for velocity include a flat velocity profile at the inlet; slip conditions at top, bottom, front, back and outlet surfaces; and a

Table 2. Domain size and fluid and particle properties of simulations

Domain Dimensions	
Width (x–dir)	4 m
Transverse thickness (y–dir)	4 m
Height (z–dir)	10 m
Grid (x × y × z)	16 × 16 × 40
Particle properties	
Number of particles	400
Diameter (D_p)	2 mm
Density (ρ_p)	50 $\mathrm{kg\,m^{-3}}$
Fluid properties (at 0 °C)	
Viscosity (μ)	1.34 $\times 10^{-5}$ $\mathrm{m^2\,s^{-1}}$
Density (ρ_f)	1.284 $\mathrm{kg\,m^{-3}}$

no-slip condition at the object (MASC). Zero gradient pressure fields are applied at all boundaries. The flow is allowed to reach steady-state prior to tracking particles through a “frozen" flow field.

In simulations of the response of the particles to horizontal winds in the vicinity of the MASC, the particles are evenly distributed on a 20×20 grid with 1 mm spacing in the x–direction and 2 mm spacing in the y–direction. The particles fall downward at an initial velocity of $1\,\mathrm{m\,s^{-1}}$ from an initial height of $3\,\mathrm{m}$ above the MASC in the $-z$ direction under the force of gravity, reaching an average terminal velocity of $1.05\,\mathrm{m\,s^{-1}}$ well before encountering flows perturbed by the MASC. Initial particle positions are ∼2 to 20 m away from the MASC in the upstream horizontal direction, depending on the flow velocity. These initial positions were evaluated to ensure the particles fell into the center of the aperture. An example of simulated particle trajectories is shown in Fig. 12.

Figure 13 shows interactions of a horizontal flow in the +y direction of 1 $\mathrm{m\,s^{-1}}$ with the MASC body. There is a clear separation of flow at the upstream side of the aperture, a relatively large upward component above the aperture at the upstream side, and a smaller downward component within the aperture. The fall speeds of particles carried into the aperture by the prevailing flow are decreased by this upward component of the flow, which increases with increasing wind speeds.

The response of particles to these perturbations for horizontal winds in both the $-x$ and $+y$ directions is shown in Fig. 14. The mean particle fall speed within the MASC aperture decreases from $1.07\,(1.04)\,\mathrm{m\,s^{-1}}$ to $0.30\,(0.26)\,\mathrm{m\,s^{-1}}$ as the ambient wind speed increases from 1 to $10\,\mathrm{m\,s^{-1}}$ (Table 3). Although there is little difference between the wind directions shown in Fig. 14, particles carried by flow in the $+x$ direction were mostly blocked by the LEDs located on top of the MASC, especially for speeds of $> 2\,\mathrm{m\,s^{-1}}$ (not shown).

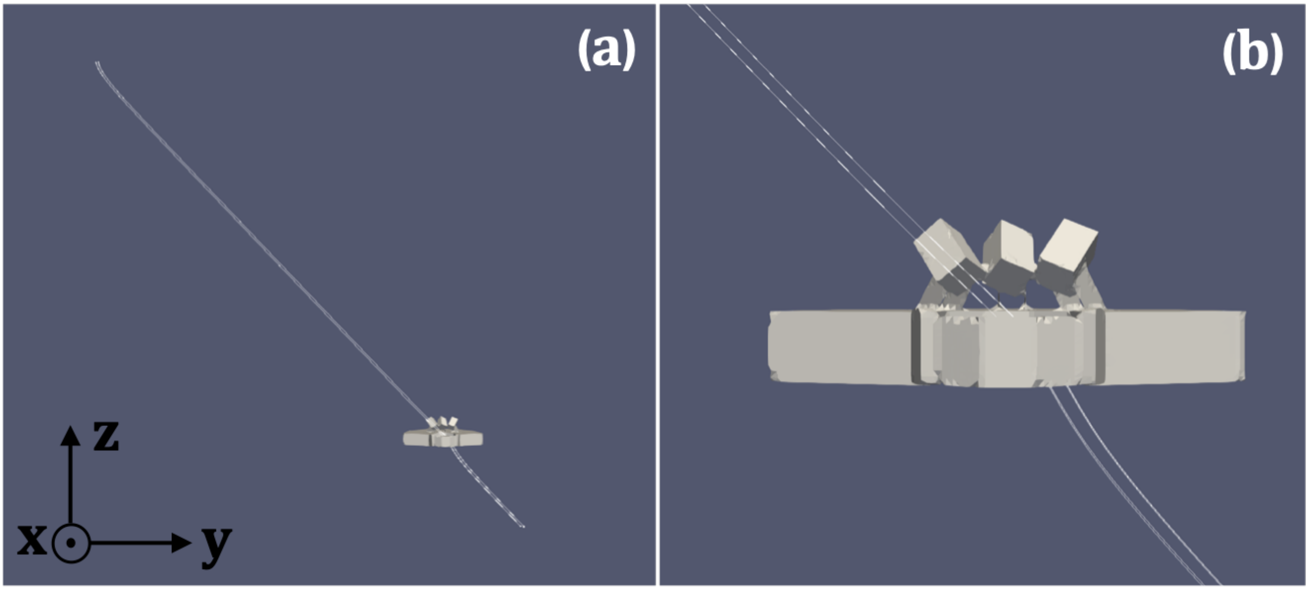

Figure 12. Example of simulated particle trajectories for a horizontal wind speed of $1\,\mathrm{m\,s^{-1}}$

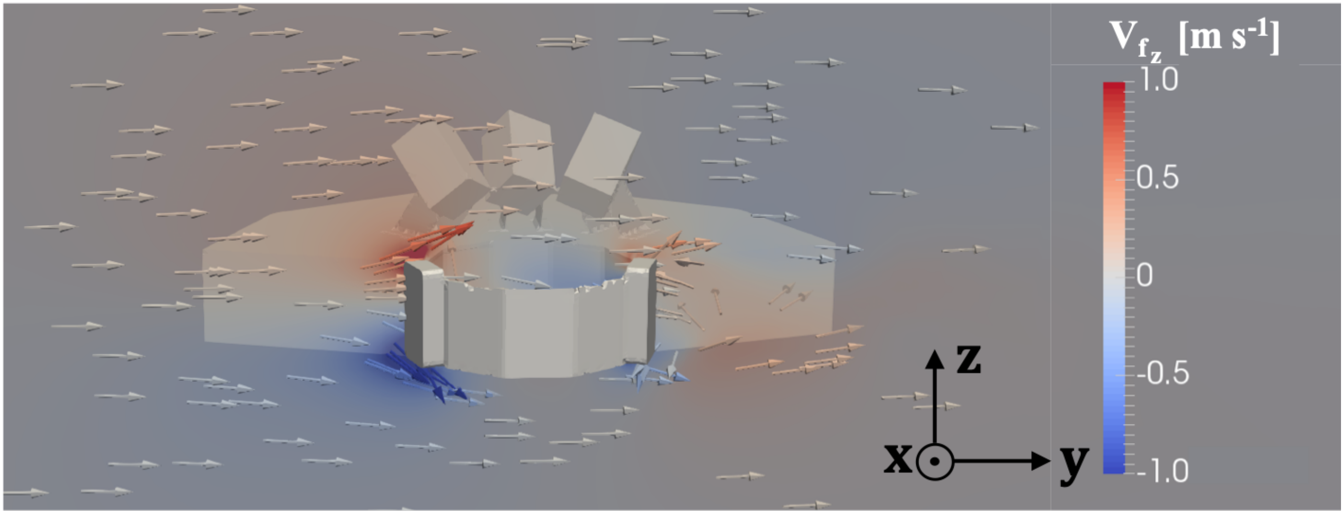

Figure 13. Simulated wind field around the MASC with undisturbed winds set at $1\,\mathrm{m\,s^{-1}}$ towards the +y direction. Color represents the vertical wind speed v_{f_z}, and arrows show wind directions on the y–z plane. The plane in which the arrows are located is aligned with the center of the aperture on the y–z plane, and x–positive points out of the page.

The influence of ambient turbulent intensity expressed as $TKE = \frac{1}{2}(\overline{v'_{f_x}}^2 + \overline{v'_{f_y}}^2 + \overline{v'_{f_z}}^2)$ was calculated for $TKE = 1$, 3, and 5 $\mathrm{m^2\,s^{-2}}$, where the perturbation velocity v'_f is the difference between the instantaneous and average velocities of the

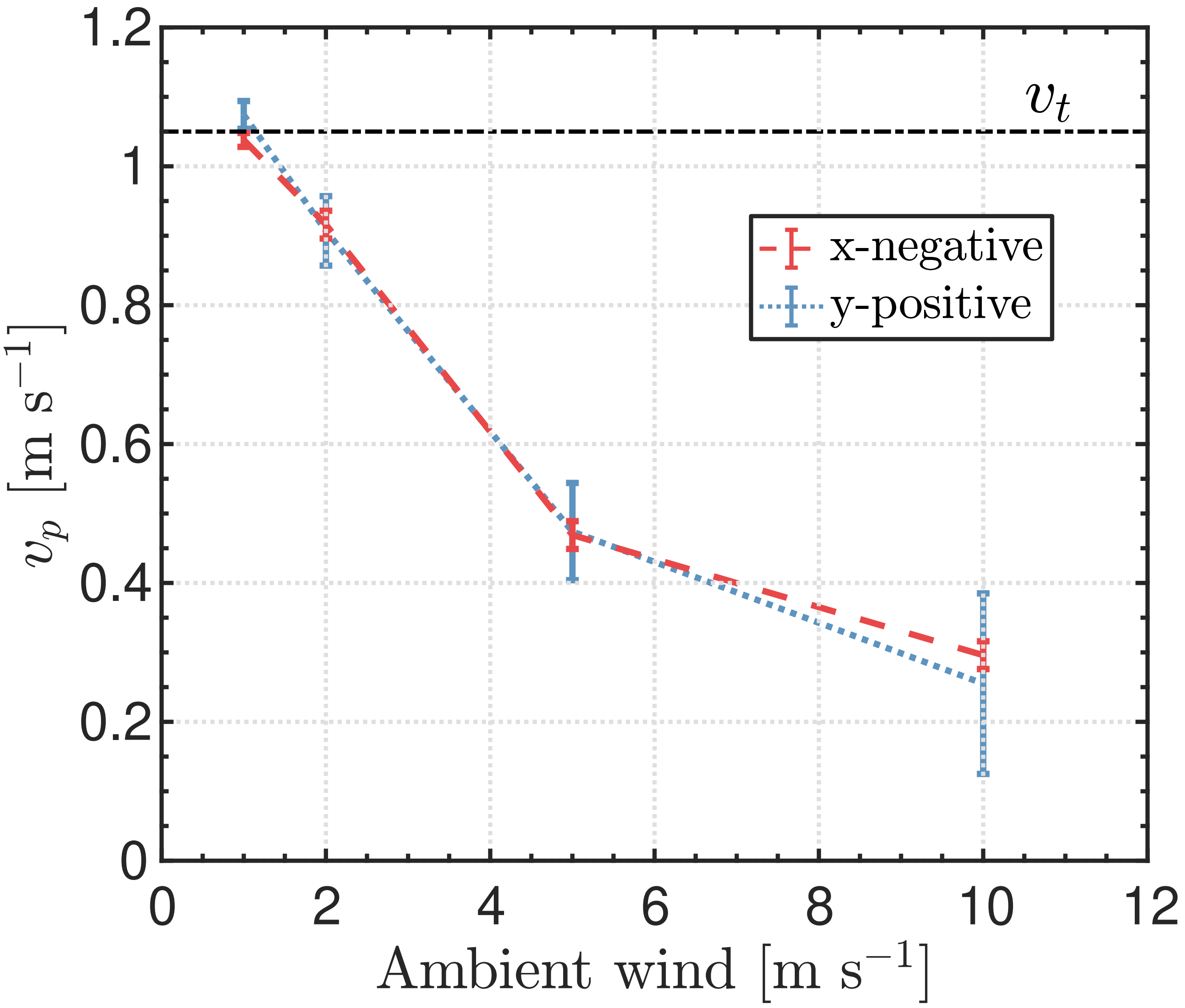

Figure 14. Mean fall speed of particles v_p as a function of ambient wind speed. Error bars represent the standard deviation of all the particles at each ambient wind speed. x–negative and y–positive represent the wind pointing towards $-x$ and $+y$ directions (see Fig. 11(d)), respectively. Terminal fall speed v_t is included for comparison, and the initial TKE is $1\,\mathrm{m}^2\,\mathrm{s}^{-2}$. Data are sampled at the center of the aperture.

atmospheric flow. These TKE values are used as initial conditions in the k–ω–SST closure model, which determines the shear stress, which in turn is used in the momentum budget equation. Figure 15 shows that for a wind speed of $10\,\mathrm{m\,s^{-1}}$, the mean particle fall speed is 24% lower for an initial value of $TKE = 1\,\mathrm{m}^2\,\mathrm{s}^{-2}$ than it is for $TKE = 5\,\mathrm{m}^2\,\mathrm{s}^{-2}$ (Table 3).

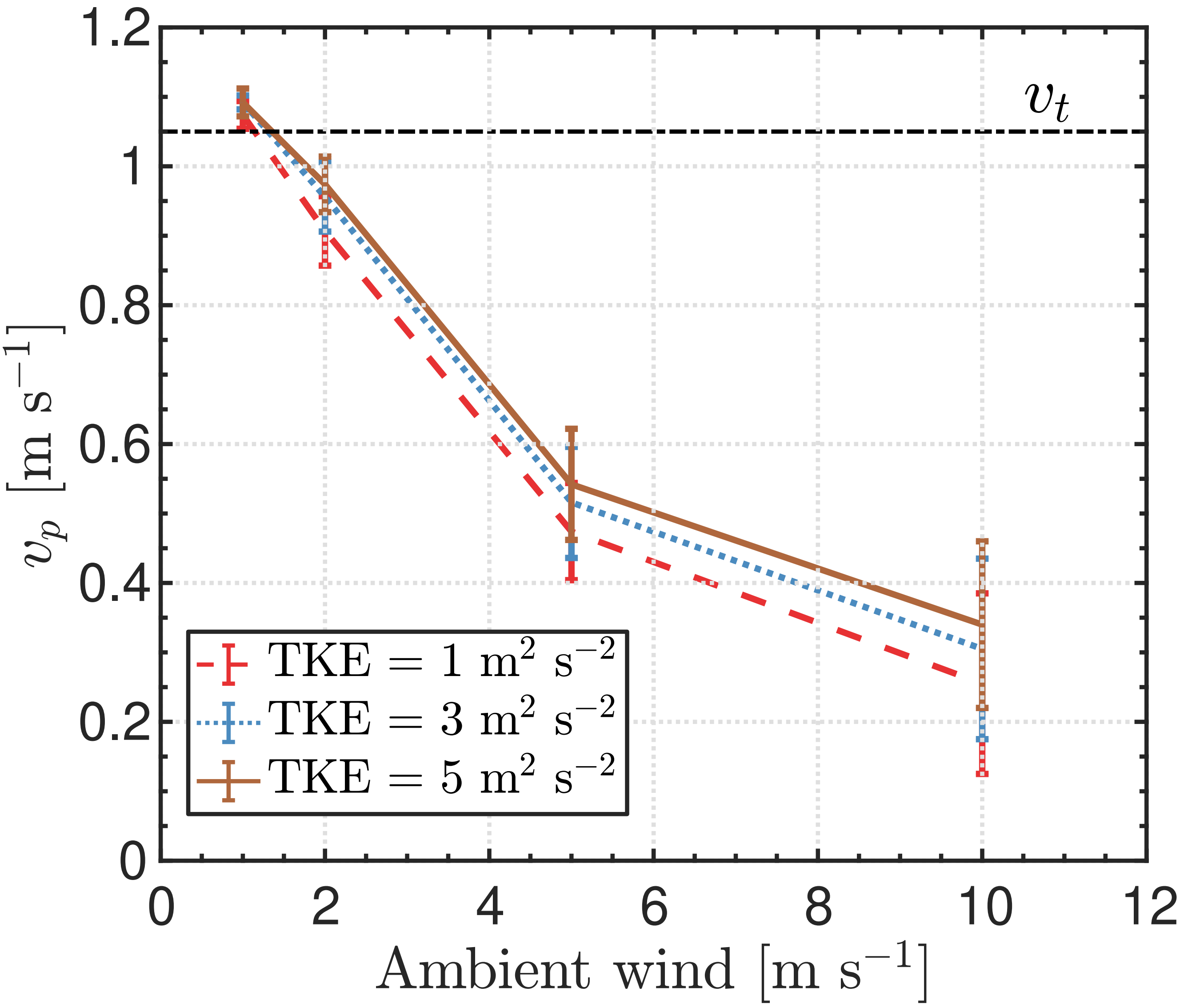

Figure 15. Mean fall speed v_p of particles versus ambient wind speed for different values of initial TKE. Terminal fall speed v_t is included for comparison. Data are sampled at the center of the aperture.

4 Discussion

The cutoff fall speed v_c defined in Sect. 2.2 is a potentially useful threshold for quality control of MASC fall speed measurements, and Fig. 5 suggests that $v_c = v_c(U_{sfc})$ for shielded MASC measurements. Least squares linear regression fits of v_c to U_{sfc} are plotted in Fig. 16 in increments of 0.5 $\mathrm{m\,s^{-1}}$. Goodness-of-fit is 0.95 or greater for all but the most heavily rimed particles, where a value of 0 indicates no relationship, and 1 indicates a perfect relationship. Data points tend to fall outside the

Table 3. Mean particle fall speed for various wind directions, wind speeds, and TKE values. The terminal fall speed is 1.05 $\mathrm{m\,s^{-1}}$ in all runs.

Ambient wind	**1** $\mathrm{m\,s^{-1}}$	**2** $\mathrm{m\,s^{-1}}$	**5** $\mathrm{m\,s^{-1}}$	**10** $\mathrm{m\,s^{-1}}$
Wind Direction				
x-negative	1.07 $\mathrm{m\,s^{-1}}$	0.92 $\mathrm{m\,s^{-1}}$	0.47 $\mathrm{m\,s^{-1}}$	0.30 $\mathrm{m\,s^{-1}}$
y-positive	1.04 $\mathrm{m\,s^{-1}}$	0.91 $\mathrm{m\,s^{-1}}$	0.47 $\mathrm{m\,s^{-1}}$	0.26 $\mathrm{m\,s^{-1}}$
TKE				
1 $\mathrm{m^2\,s^{-2}}$	1.07 $\mathrm{m\,s^{-1}}$	0.91 $\mathrm{m\,s^{-1}}$	0.47 $\mathrm{m\,s^{-1}}$	0.26 $\mathrm{m\,s^{-1}}$
3 $\mathrm{m^2\,s^{-2}}$	1.09 $\mathrm{m\,s^{-1}}$	0.96 $\mathrm{m\,s^{-1}}$	0.52 $\mathrm{m\,s^{-1}}$	0.31 $\mathrm{m\,s^{-1}}$
5 $\mathrm{m^2\,s^{-2}}$	1.09 $\mathrm{m\,s^{-1}}$	0.98 $\mathrm{m\,s^{-1}}$	0.54 $\mathrm{m\,s^{-1}}$	0.34 $\mathrm{m\,s^{-1}}$

95% confidence interval for the most restricted wind speeds ($U_{sfc} < 2\,\mathrm{m\,s^{-1}}$, or $< 4\,\mathrm{m\,s^{-1}}$ for graupel), corresponding to the lowest number of observations. These fits can be used as a guide for quality control of shielded MASC measurements, where particles with fall speeds below v_c are either omitted or corrected through extrapolation.

For unshielded MASC measurements, the simulations show that the separation of flow leads to an upward flow velocity component above the aperture that tends to decrease the mean fall speed of particles falling into the aperture (Figs. 14 and 15). As wind speed increases, the mean simulated fall speed decreases, and values do not deviate substantially from the mean (Figs. A1 through A4). In contrast, unshielded measurements of fall speed are highly skewed towards low values (Figs. 5(a) and (b)) and the distribution is bimodal for the lightest winds (Fig. 5(c)). Therefore, while the primary effect of perturbed winds slowing particle fall speeds is generally well represented in the simulations, the details appear to be more complicated in reality.

Larger aggregates with negligible riming tend to be more susceptible than smaller, more dense particles to disturbance by surface winds and associated turbulence, with a tendency for more vertical orientations ~~and~~ (Fig. 8), slower fall speeds (Fig. 6), and with a lower frequency of occurrence ~~than~~ at higher wind speeds (Table 1) than for other riming classes. ~~This finding supports that of Thériault et al. (2012), who found that faster-falling hydrometeors are collected more efficiently by~~ The Stokes number is defined as the dimensionless ratio of the particle relaxation time to its terminal velocity in still air v_t/g, and a characteristic time of isotropic, homogeneous turbulent flow. Snowflakes with low Stokes numbers tend to follow the flow, becoming trapped in the vortices with the orientation aligning with the local velocity gradient (Voth and Soldati, 2017). The implication is that large, low-density, aggregate-type hydrometeors — with relatively small values of v_t compared to more heavily rimed particles — have low values of the Stokes number and are more likely to follow the motions of any turbulent flow induced by the MASC aperture. This finding is consistent with prior work by Thériault et al. (2012) who showed that for a Geonor gauge inside a single Alter shield~~. Therefore~~, higher-density, faster-falling hydrometeors are collected most efficiently.

The implication is that particle type needs to be considered when accounting for the effect of wind speed on snow measurements. However, the collection efficiencies for all riming classes sampled in the present study are found to be highly sensitive

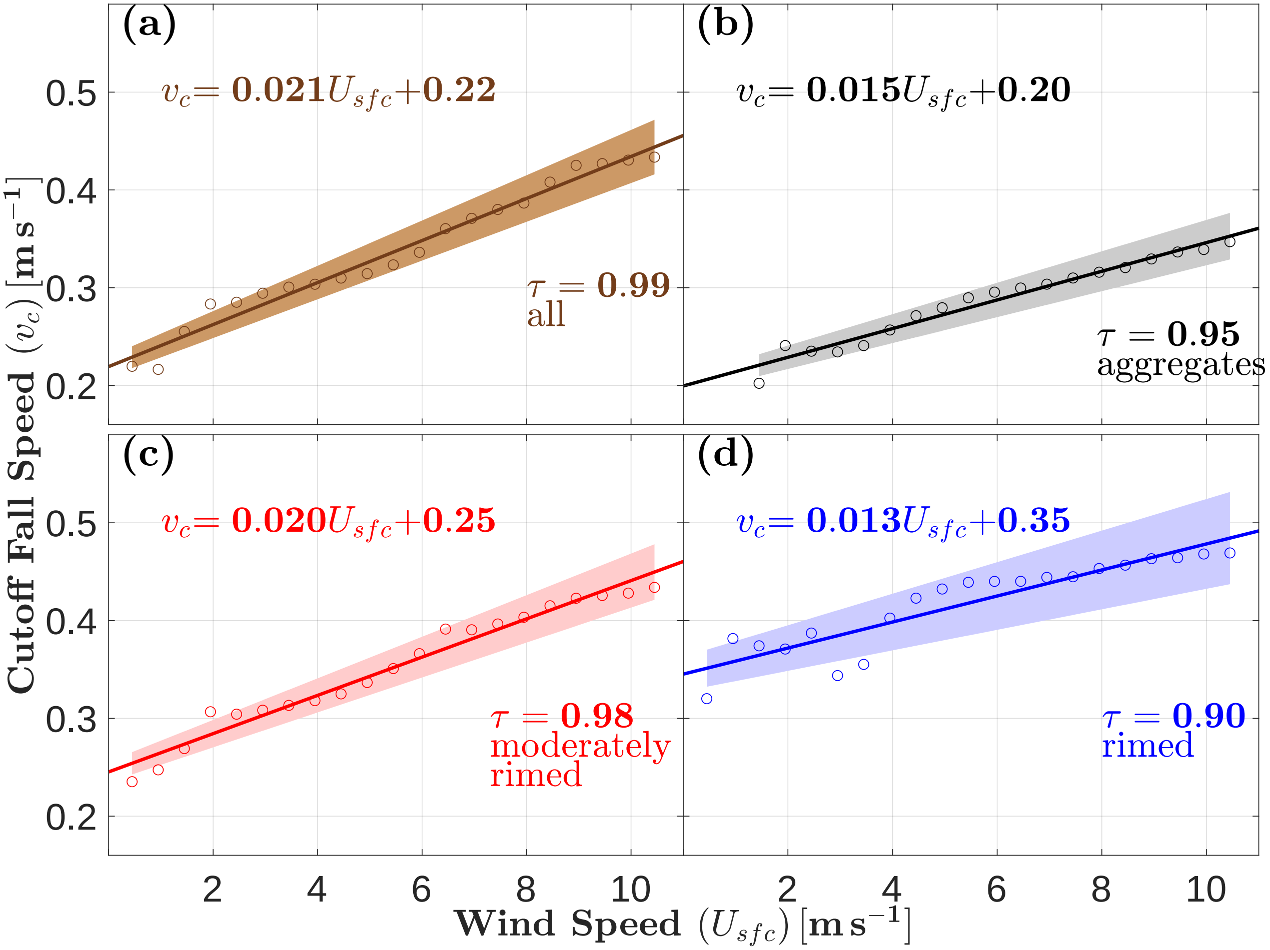

Figure 16. Cutoff MASC fall speed v_c, defined in Sect. 2.2, as a function of surface wind speed U_{sfc} for (a) all hydrometeor types, (b) aggregates, (c) moderately rimed, and (d) rimed. The solid line in each subplot is a linear least squares best fit, while the shaded regions bound the 95% confidence interval. Goodness-of-fit is measured by applying the Kendall rank correlation coefficient $\tau = 2(P-Q)/n(n-1)$ (Kendall, 1938), where P is the number of concordant pairs, Q is the number of discordant pairs, and n is the total number of pairs. A value of $\tau = 0$ indicates no relationship and 1 indicates a perfect relationship. The confidence interval represents the range of error for predicting a new value for v_c. Only shielded MASC measurements are shown.

to winds in the absence of a wind shield. This sensitivity is reduced but still apparent for all but perhaps the very lightest winds $U_{sfc} \leq 0.5\,\mathrm{m\,s^{-1}}$, even when located inside of a double wind fence. This is likely the result of upstream turbulence propagating into the collection area as a result of wind interacting with shield deflector fins, as suggested in Colli et al. (2016a, b).

~~Prior MASC observations (Garrett and Yuter, 2014) and work by Nielsen (2007) have shown that fall speed distributions are broadened in highly turbulent flows, where fall speeds are either enhanced are reduced by turbulent eddies. Considering also~~ Considering that the MASC observes one hydrometeor at a time, while the KAZR fall speed is the mean value from a volume of scattering hydrometeors, it is certainly possible that at least some of the measurements comprising the low-fall-speed mode of the MASC fall speed distributions are a natural result of turbulence and not caused by the interaction of surface winds with the MASC or MASC-shield configuration. However, without more direct fall speed measurements to compare with, the highest confidence in the MASC fall speed measurements is achieved by omitting measured fall speeds that fall below v_c.

For particle values derived from MASC images, the average of all three images was used. An average is not the best guess for the true orientation angle in all cases. For example, depending on the azimuthal orientation with respect to the central camera, the particle's major axis may not be resolved entirely. Jiang et al. (2019) showed that the azimuthal orientation is correlated with the wind direction, with particles' major axes tending to align with the wind direction. In our case, this would imply that the major axis was often oriented such that it was not entirely resolved by any of the three cameras. More work needs to be done to investigate the limitations of the MASC-determined orientation angle.

5 Conclusions

Accurate measurement of solid hydrometeor fall speed, orientation, and size distribution is critical for constraining numerical model parameterizations and remote sensing retrievals. Surface winds are known to have a strong influence on the collection of solid hydrometeors that is dependent on the specific gauge-shield configuration. ~~Simulations of wind interactions with an unshielded MASC showed an average reduction in mean particle fall speed of 74% for winds increasing to $10\,\mathrm{m\,s^{-1}}$, while TKE had only a weak, inverse effect on the reduction.~~ In comparison with coincident KAZR observations of mean Doppler velocity, MASC measurements of fall speed were in closest agreement only when ~~both~~ the MASC was shielded with a double wind fence and winds were light ($U_{sfc} \leq 5\,\mathrm{m\,s^{-1}}$). For the lightest wind speeds ($U_{sfc} \leq 1.5\,\mathrm{m\,s^{-1}}$), shielded measurements of orientation angles decreased to a mode of $12\,°$, and concentrations of sparsely-rimed aggregates with $D_{max} \simeq 7\,\mathrm{mm}$ increased by a factor of five. However, we showed that even in these wind-restricted and shielded cases, a fraction of MASC-measured fall speeds ~~–~~— those below a wind-speed-dependent cutoff fall speed that is most often $v_c \lesssim 0.5$ ~~–~~— still do not match KAZR measurements. We showed that this cutoff fall speed is a function of wind speed for shielded observations and provided linear regression fits that can be used for additional quality control of MASC measurements.

Simulations of wind interactions with an unshielded MASC yielded an average reduction in mean particle fall speed of 74% for winds increasing to $10\,\mathrm{m\,s^{-1}}$, while TKE had only a weak, inverse effect on the reduction. The simulations revealed that an upward component of perturbed flow at the upstream side of the MASC aperture increases in magnitude with increased wind speed, which in turn leads to a decreased mean particle fall speed.

Relatively simple simulations were carried out here to support the findings of the observations analyses. We used only a single set of particles with limited, yet representative characteristics to support observations analyses with simulated particle responses to MASC-perturbed flow. Future work could include a much more diverse set of particle shapes, sizes, and densities, as well as a turbulent dispersion model and other forces that have been neglected in this work. Furthermore, a double wind fence ~~in the CFD simulation~~ should be included in future CFD simulations of flow in and around the MASC to see more precisely how the wind field evolves as it encounters the individual deflector fins in each portion of the fence~~, where these fins are allowed to move with the wind~~. Thériault et al. (2012) simulated the wind field for a Geonor gauge with a single Alter shield by accounting for the movement of deflector fins on the upstream side of the gauge, where fins were assigned angles with respect to the vertical that increased as a function of wind speed. Such careful simulation might improve the fidelity of wind-shield-gauge influence on snow measurements.

The intent of this work is to provide guidance for under what measurement conditions the MASC can be used to obtain accurate information about hydrometeor microphysical properties and fall speeds. However, those conditions are limited to measurements within still air. The distributions of ~~frozen~~ solid hydrometeor size, type, orientation, and fall speed in natural, turbulent air remain to be determined.

Appendix A: Simulated particle fall speed distributions

Figures A1, A2, A3, and A4 show simulated particle fall speed distributions for horizontal wind speeds of 1, 2, 5, and $10\,\mathrm{m\,s^{-1}}$, respectively.

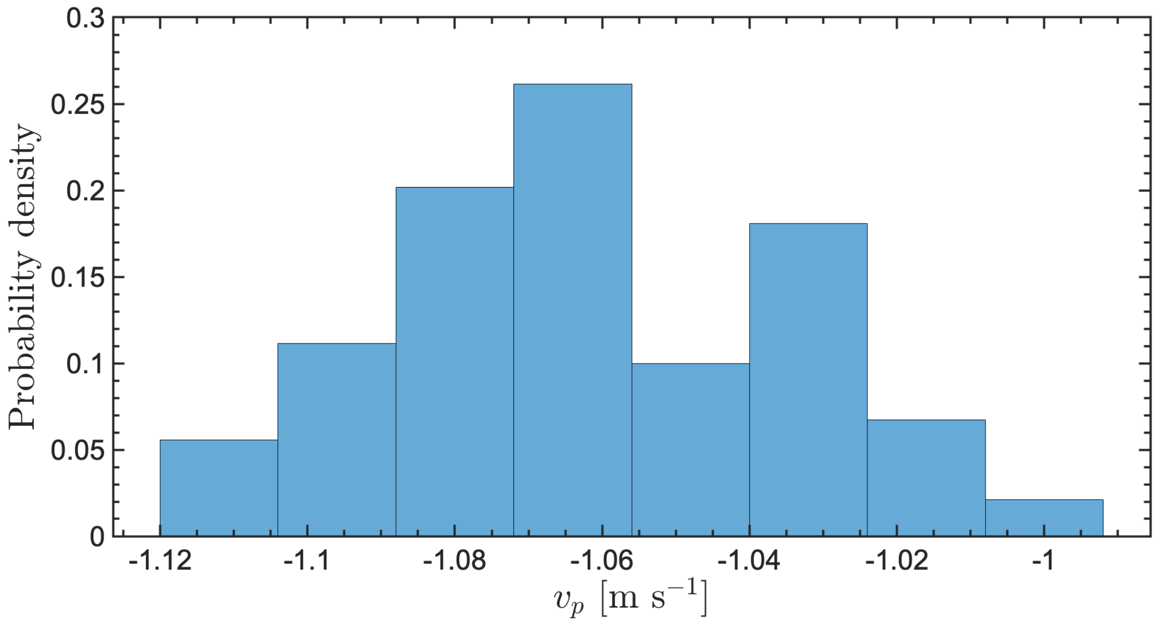

Figure A1. Simulated particle fall speed distributions for a horizontal wind speed of $1\,\mathrm{m\,s^{-1}}$

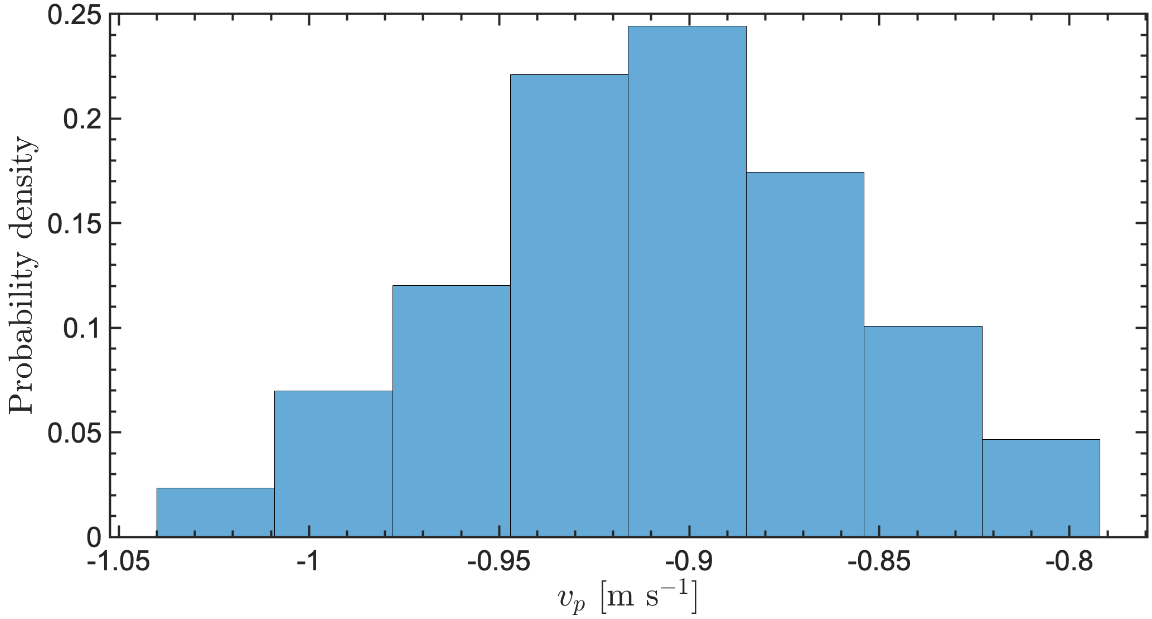

Figure A2. Simulated particle fall speed distributions for a horizontal wind speed of $2\,\mathrm{m\,s^{-1}}$

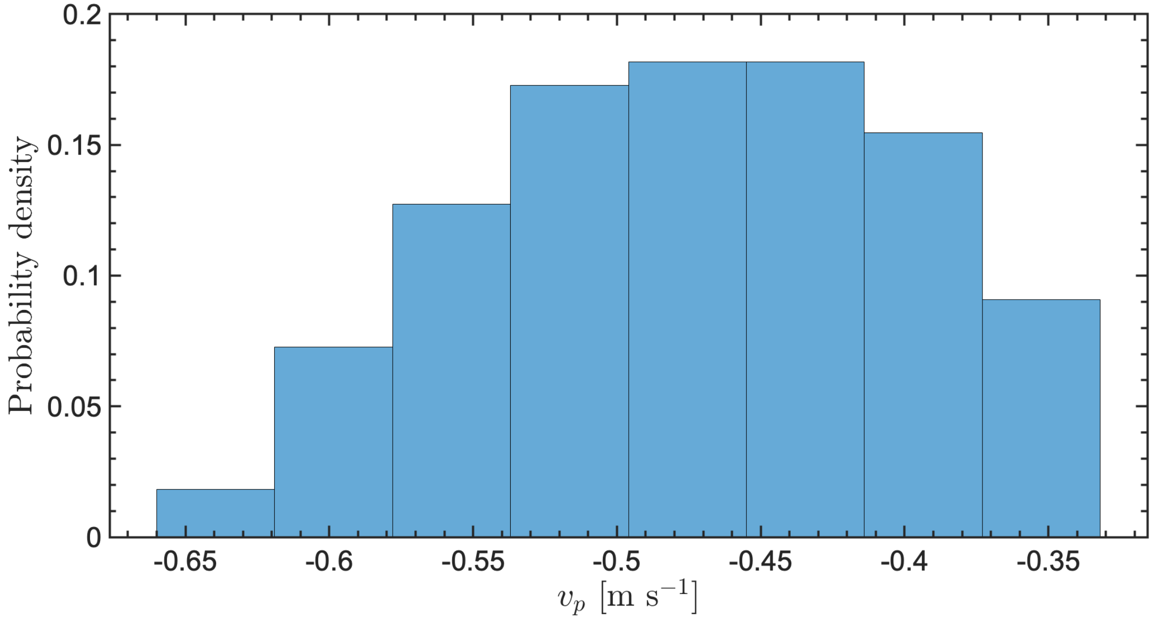

Figure A3. Simulated particle fall speed distributions for a horizontal wind speed of $5\,\mathrm{m\,s^{-1}}$

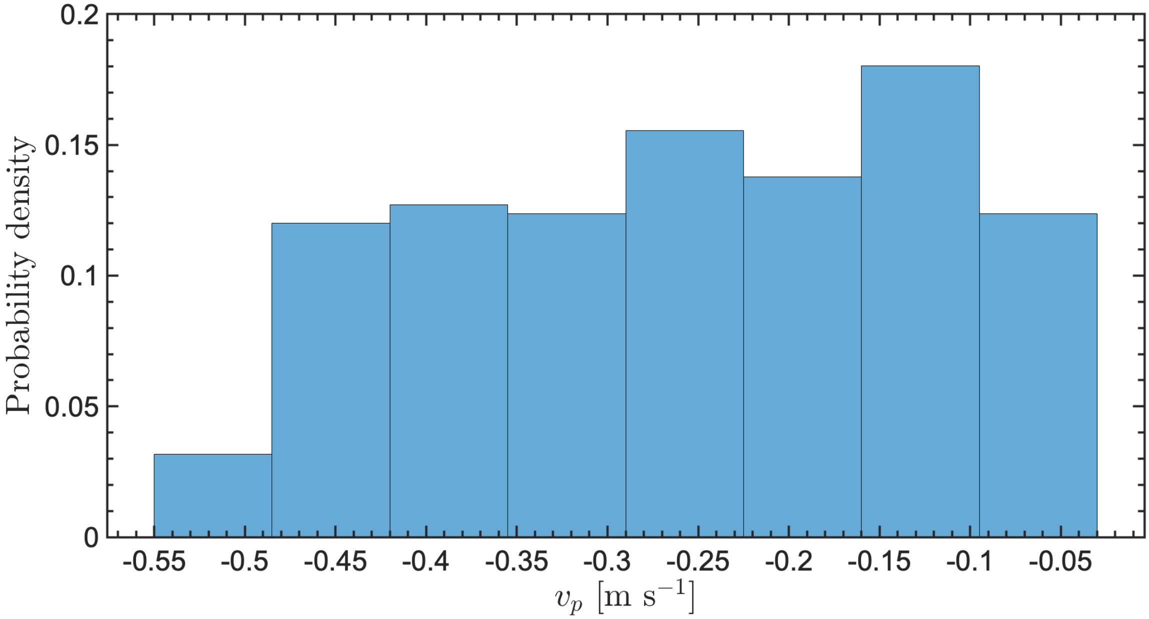

Figure A4. Simulated particle fall speed distributions for a horizontal wind speed of $10\,\mathrm{m\,s^{-1}}$

Code and data availability. The code and data supporting this project are available at https://doi.org/10.7278/S50DQTX9K7QY. This repository includes code sufficient to replicate the observations analysis results. Raw and processed MASC data are available from the ARM data archive at https://adc.arm.gov/discovery/#/, and raw MASC data can be processed with the *mascpy* code located at https://doi.org/10.7278/S50DVA5JK2PD. OpenFoam v4.1 software is available at https://openfoam.org/version/4-1/.

Author contributions. All authors contributed to the formulation of the project. KF and TG developed the methodology and software code for observations analysis. CH developed the methodology and software implementation for the simulations, with AT advising. KF and CH wrote the article with contributions from TG and AT.

Competing interests. TG is co-owner and scientific advisor of Particle Flux Analytics, Inc., the company manufacturing the Multi-Angle Snowflake Camera. Otherwise, the authors declare that they have no conflict of interest.

Acknowledgements. This work was supported by the Department of Energy Atmospheric System Research program Grant DE-SC0016282 and the National Science Foundation (NSF) Physical and Dynamic Meteorology program award number 1841870. We thank Krista Gaustad and Martin Stuefer for sharing ~~precise~~ dates, locations, and ~~orientations~~ deployment details of the instrument and wind shield. We also thank Silvio Schmalfuß and two anonymous reviewers for their comments and questions, which have improved this work substantially.

References

ARM Climate Research Facility: Surface Meteorological Instrumentation (MET), 2014-11-11 to 2018-09-09, ARM Mobile Facility (OLI) Oliktok Point, Alaska; AMF3 (M1). Compiled by M. Ritsche, J. Kyrouac, N. Hickmon and D. Holdridge. ARM Data Center: Oak Ridge, Tennessee, USA. Data set accessed 2019-10-09 at http://dx.doi.org/10.5439/1025220, 2013.

ARM Climate Research Facility: Multi-Angle Snowflake Camera (MASC), 2015-11-29 to 2018-08-28, ARM Mobile Facility (OLI) Oliktok Point, Alaska; AMF3 (M1). Compiled by B. Ermold, K. Shkurko, and M. Stuefer. ARM Data Center: Oak Ridge, Tennessee, USA. Data set accessed 2018-09-26 at http://dx.doi.org/10.5439/1234550, 2014.

ARM Climate Research Facility: Active Remote Sensing of CLouds (ARSCL) product using Ka-band ARM Zenith Radars (ARSCLKAZR1KOLLIAS), 2015-11-29 to 2018-09-10, ARM Mobile Facility (OLI) Oliktok Point, Alaska; AMF3 (M1). Compiled by Compiled by K. Johnson, T. Toto and S. Giangrande. ARM Data Center: Oak Ridge, Tennessee, USA. Data set accessed 2019-10-14 at http://dx.doi.org/10.5439/1350629, 2015.

Balogh, M., Parente, A., and Benocci, C.: RANS simulation of ABL flow over complex terrains applying an Enhanced k-ε model and wall function formulation: Implementation and comparison for fluent and OpenFOAM, Journal of Wind Engineering and Industrial Aerodynamics, 104, 360–368, 2012.

Besic, N., Gehring, J., Praz, C., Figueras i Ventura, J., Grazioli, J., Gabella, M., Germann, U., and Berne, A.: Unraveling hydrometeor mixtures in polarimetric radar measurements, Atmospheric Measurement Techniques, 11, 4847–4866, https://doi.org/10.5194/amt-11-4847-2018, 2018.

Böhm, H. P.: A general equation for the terminal fall speed of solid hydrometeors, Journal of the Atmospheric Sciences, 46, 2419–2427, https://doi.org/10.1175/1520-0469(1989)046%3C2419:AGEFTT%3E2.0.CO;2, 1989.

Bowman, A. W. and Azzalini, A.: Applied Smoothing Techniques for Data Analysis, Oxford University Press, Inc., New York, https://doi.org/10.1007/s001800000033, 1997.

Bringi, V., Kennedy, P., Huang, G.-J., Kleinkort, C., Thurai, M., and Notaroš, B.: Dual-polarized radar and surface observations of a winter graupel shower with negative Z dr column, Journal of Applied Meteorology and Climatology, 56, 455–470, https://doi.org/10.1175/JAMC-D-16-0197.1, 2017.

Caretto, L., Gosman, A., Patankar, S., and Spalding, D.: Two calculation procedures for steady, three-dimensional flows with recirculation, in: Proceedings of the third international conference on numerical methods in fluid mechanics, pp. 60–68, Springer, https://doi.org/10.1007/BFb0112677, 1973.

Chen, G., Xiong, Q., Morris, P. J., Paterson, E. G., Sergeev, A., and Wang, Y.: OpenFOAM for computational fluid dynamics, Notices of the AMS, 61, 354–363, https://doi.org/10.1090/noti1095, 2014.

Clothiaux, E. E., Ackerman, T. P., Mace, G. G., Moran, K. P., Marchand, R. T., Miller, M. A., and Martner, B. E.: Objective determination of cloud heights and radar reflectivities using a combination of active remote sensors at the ARM CART sites, Journal of Applied Meteorology, 39, https://doi.org/10.1175/1520-0450(2000)039%3C0645:ODOCHA%3E2.0.CO;2, 2000.

Colli, M., Rasmussen, R., Thériault, J. M., Lanza, L. G., Baker, C. B., and Kochendorfer, J.: An improved trajectory model to evaluate the collection performance of snow gauges, Journal of Applied Meteorology and Climatology, 54, 1826–1836, https://doi.org/10.1175/JAMC-D-15-0035.1, 2015.

Colli, M., Lanza, L. G., Rasmussen, R., and Thériault, J. M.: The collection efficiency of shielded and unshielded precipitation gauges. Part I: CFD airflow modeling, Journal of Hydrometeorology, 17, 231–243, https://doi.org/10.1175/JHM-D-15-0010.1, 2016a.

Colli, M., Lanza, L. G., Rasmussen, R., and Thériault, J. M.: The collection efficiency of shielded and unshielded precipitation gauges. Part II: Modeling particle trajectories, Journal of Hydrometeorology, 17, 245–255, https://doi.org/10.1175/JHM-D-15-0011.1, 2016b.

Cooper, S. J., Wood, N. B., and L'Ecuyer, T. S.: A variational technique to estimate snowfall rate from coincident radar, snowflake, and fall-speed observations, Atmospheric Measurement Techniques (Online), 10, https://doi.org/10.5194/amt-10-2557-2017, 2017.

Dehbi, A.: A CFD model for particle dispersion in turbulent boundary layer flows, Nuclear Engineering and Design, 238, 707–715, https://doi.org/10.1016/j.nucengdes.2007.02.055, 2008.

Dunnavan, E. L., Jiang, Z., Harrington, J. Y., Verlinde, J., Fitch, K., and Garrett, T. J.: The Shape and Density Evolution of Snow Aggregates, Journal of the Atmospheric Sciences, 76, 3919–3940, https://doi.org/10.1175/JAS-D-19-0066.1, 2019.

Elghobashi, S.: On predicting particle-laden turbulent flows, Applied Scientific Research, 52, 309–329, https://doi.org/10.1007/BF00936835, 1994.

Ferrari, G., Federici, D., Schito, P., Inzoli, F., and Mereu, R.: CFD study of Savonius wind turbine: 3D model validation and parametric analysis, Renewable Energy, 105, 722–734, https://doi.org/10.1016/j.renene.2016.12.077, 2017.

Flato, G., Marotzke, J., Abiodun, B., Braconnot, P., Chou, S., Collins, W., Cox, P., Driouech, F., Emori, S., Eyring, V., Forest, C., Gleckler, P., Guilyardi, E., Jakob, C., Kattsov, V., Reason, C., and Rummukainen, M.: Evaluation of Climate Models, book section 9, p. 820, Cambridge University Press, Cambridge, United Kingdom and New York, NY, USA, https://doi.org/https://doi.org/10.1017/CBO9781107415324.020, www.climatechange2013.org, 2013.

Garrett, T. J. and Yuter, S. E.: Observed influence of riming, temperature, and turbulence on the fallspeed of solid precipitation, Geophysical Research Letters, 41, 6515–6522, https://doi.org/10.1002/2014GL061016, 2014.

Garrett, T. J., Fallgatter, C., Shkurko, K., and Howlett, D.: Fall speed measurement and high-resolution multi-angle photography of hydrometeors in free fall, Atmospheric Measurement Techniques, 5, 2625–2633, https://doi.org/10.5194/amt-5-2625-2012, 2012.

Garrett, T. J., Yuter, S. E., Fallgatter, C., Shkurko, K., Rhodes, S. R., and Endries, J. L.: Orientations and aspect ratios of falling snow, Geophysical Research Letters, 42, 4617–4622, https://doi.org/10.1002/2015GL064040, 2015.

Gergely, M. and Garrett, T. J.: Impact of the natural variability in snowflake diameter, aspect ratio, and orientation on modeled snowfall radar reflectivity, Journal of Geophysical Research: Atmospheres, 121, 12–236, https://doi.org/10.1002/2016JD025192, 2016.

Gergely, M., Cooper, S. J., and Garrett, T. J.: Using snowflake surface-area-to-volume ratio to model and interpret snowfall triple-frequency radar signatures, Atmospheric Chemistry and Physics (Online), 17, https://doi.org/10.5194/acp-17-12011-2017, 2017.

Gisen, D.: Generation of a 3D mesh using snappyHexMesh featuring anisotropic refinement and near-wall layers, in: ICHE 2014. Proceedings of the 11th International Conference on Hydroscience & Engineering, pp. 983–990, 2014.

Goodison, B. E., Louie, P. Y. T., and Yang, D.: WMO Solid Precipitation Measurement Intercomparison, report WMO/TD No. 872, World Meteorological Organization, 1998.

Grazioli, J., Genthon, C., Boudevillain, B., Duran-Alarcon, C., Del Guasta, M., Madeleine, J.-B., and Berne, A.: Measurements of precipitation in Dumont d'Urville, Adélie Land, East Antarctica, Cryosphere, 11, 1797–1811, https://doi.org/10.5194/tc-11-1797-2017, 2017.

Greenshields, C. J.: OpenFOAM User Guide, FM Global, v3.0.1, 2015.

Groisman, P. Y. and Legates, D. R.: The accuracy of United States precipitation data, Bulletin of the American Meteorological Society, 75, 215–228, https://doi.org/10.1175/1520-0477(1994)075<0215:TAOUSP>2.0.CO;2, 1994.

Groisman, P. Y., Koknaeva, V. V., Belokrylova, T. A., and Karl, T. R.: Overcoming biases of precipitation measurement: A history of the USSR experience, Bulletin of the American Meteorological Society, 72, 1725–1733, https://doi.org/10.1175/1520-0477(1991)072<1725:OBOPMA>2.0.CO;2, 1991.

Hicks, A. and Notaroš, B.: Method for Classification of Snowflakes Based on Images by a Multi-Angle Snowflake Camera Using Convolutional Neural Networks, Journal of Atmospheric and Oceanic Technology, 36, 2267–2282, https://doi.org/10.1175/JTECH-D-19-0055.1, 2019.

Higuera, P., Lara, J. L., and Losada, I. J.: Three-dimensional interaction of waves and porous coastal structures using OpenFOAM®. Part I: formulation and validation, Coastal Engineering, 83, 243–258, https://doi.org/10.1016/j.coastaleng.2013.08.010, 2014.

Huang, G.-J., Kleinkort, C., Bringi, V., and Notaroš, B. M.: Winter precipitation particle size distribution measurement by Multi-Angle Snowflake Camera, Atmospheric Research, 198, 81–96, https://doi.org/10.1016/j.atmosres.2017.08.005, 2017.

Iudiciani, P.: Lagrangian particle tracking of spheres and cylinders, Chalmers University of Technology, 2009.

Jasak, H., Jemcov, A., and Tukovic, Z.: OpenFOAM : A C ++ Library for Complex Physics Simulations, International Workshop on Coupled Methods in Numerical Dynamics, pp. 1–20, 2007.

Jiang, Z., Verlinde, J., Clothiaux, E. E., Aydin, K., and Schmitt, C.: Shapes and fall orientations of ice particle aggregates, Journal of the Atmospheric Sciences, 76, 1903–1916, https://doi.org/10.1175/JAS-D-18-0251.1, 2019.

Kendall, M. G.: A new measure of rank correlation, Biometrika, 30, 81–93, https://doi.org/10.1093/biomet/30.1-2.81, 1938.

Kennedy, P., Thurai, M., Praz, C., Bringi, V., Berne, A., and Notaroš, B. M.: Variations in snow crystal riming and Z DR: A case analysis, Journal of Applied Meteorology and Climatology, 57, 695–707, https://doi.org/10.1175/JAMC-D-17-0068.1, 2018.

Kim, S.-H., Ko, D.-H., Seong, D.-K., Eun, S.-H., Kim, B.-G., Kim, B.-J., Park, C.-G., and Cha, J.-W.: Quantitative Analysis of Snow Particles Using a Multi-Angle Snowflake Camera in the Yeongdong Region, Atmosphere, 29, 311–324, https://doi.org/10.14191/Atmos.2019.29.3.311, 2019.

Kim, Y.-J., Kim, B.-G., Shim, J.-K., and Choi, B.-C.: Observation and Numerical Simulation of Cold Clouds and Snow Particles in the Yeongdong Region, Asia-Pacific Journal of Atmospheric Sciences, 54, 499–510, https://doi.org/10.1007/s13143-018-0055-6, 2018.

Kleinkort, C., Huang, G.-J., Bringi, V., and Notaroš, B.: Visual hull method for realistic 3D particle shape reconstruction based on high-resolution photographs of snowflakes in free fall from multiple views, Journal of Atmospheric and Oceanic Technology, 34, 679–702, https://doi.org/10.1175/JTECH-D-16-0099.1, 2017.

Leinonen, J. and Berne, A.: Unsupervised classification of snowflake images using a generative adversarial network and K-medoids classification, Atmospheric Measurement Techniques, 13, 2949–2964, https://doi.org/10.5194/amt-13-2949-2020, 2020.

Locatelli, J. D. and Hobbs, P. V.: Fall speeds and masses of solid precipitation particles, Journal of Geophysical Research, 79, 2185–2197, https://doi.org/10.1029/JC079i015p02185, 1974.

Matrosov, S. Y.: Evaluations of the spheroidal particle model for describing cloud radar depolarization ratios of ice hydrometeors, Journal of Atmospheric and Oceanic Technology, 32, 865–879, https://doi.org/10.1175/JTECH-D-14-00115.1, 2015.

Matrosov, S. Y., Reinking, R. F., and Djalalova, I. V.: Inferring fall attitudes of pristine dendritic crystals from polarimetric radar data, Journal of the Atmospheric Sciences, 62, 241–250, https://doi.org/10.1175/JAS-3356.1, 2005.

Matrosov, S. Y., Schmitt, C. G., Maahn, M., and de Boer, G.: Atmospheric ice particle shape estimates from polarimetric radar measurements and in situ observations, Journal of Atmospheric and Oceanic Technology, 34, 2569–2587, https://doi.org/10.1175/JTECH-D-17-0111.1, 2017.

Matrosov, S. Y., Maahn, M., and De Boer, G.: Observational and modeling study of ice hydrometeor radar dual-wavelength ratios, Journal of Applied Meteorology and Climatology, 58, 2005–2017, https://doi.org/10.1175/JAMC-D-19-0018.1, 2019.

Maxey, M. R. and Riley, J. J.: Equation of motion for a small rigid sphere in a nonuniform flow, The Physics of Fluids, 26, 883–889, https://doi.org/10.1063/1.864230, 1983.

Mekis, E., Donaldson, N., Reid, J., Zucconi, A., Hoover, J., Li, Q., Nitu, R., and Melo, S.: An overview of surface-based precipitation observations at Environment and Climate Change Canada, Atmosphere-Ocean, 56, 71–95, https://doi.org/10.1080/07055900.2018.1433627, 2018.

Menter, F.: Zonal two equation k–ω turbulence models for aerodynamic flows, in: 23rd fluid dynamics, plasmadynamics, and lasers conference, p. 2906, https://doi.org/10.2514/6.1993-2906, 1993.

Moat, B. I., Yelland, M. J., Pascal, R. W., and Molland, A. F.: Quantifying the airflow distortion over merchant ships. Part I: Validation of a CFD model, Journal of Atmospheric and Oceanic Technology, 23, 341–350, https://doi.org/10.1175/JTECH1858.1, 2006.

Morrison, H. and Milbrandt, J. A.: Parameterization of cloud microphysics based on the prediction of bulk ice particle properties. Part I: Scheme description and idealized tests, Journal of the Atmospheric Sciences, 72, 287–311, https://doi.org/10.1175/JAS-D-14-0065.1, 2015.

Newman, A. J., Kucera, P. A., and Bliven, L. F.: Presenting the Snowflake Video Imager (SVI), Journal of Atmospheric and Oceanic Technology, 26, 167–179, https://doi.org/10.1175/2008JTECHA1148.1, 2009.

Nielsen, P.: Mean and variance of the velocity of solid particles in turbulence, in: Particle-Laden Flow, pp. 385–391, Springer, https://doi.org/10.1007/978-1-4020-6218-6_30, 2007.

Notaroš, B. M., Bringi, V. N., Kleinkort, C., Kennedy, P., Huang, G. J., Thurai, M., Newman, A. J., Bang, W., and Lee, G.: Accurate Characterization of Winter Precipitation Using Multi-Angle Snowflake Camera, Visual Hull, Advanced Scattering Methods and Polarimetric Radar, Atmosphere, 7, 81, https://doi.org/10.3390/atmos7060081, 2016.

Oue, M., Kollias, P., Ryzhkov, A., and Luke, E. P.: Toward exploring the synergy between cloud radar polarimetry and Doppler spectral analysis in deep cold precipitating systems in the Arctic, Journal of Geophysical Research: Atmospheres, 123, 2797–2815, https://doi.org/10.1002/2017JD027717, 2018.

Praz, C., Roulet, Y.-A., and Berne, A.: Solid hydrometeor classification and riming degree estimation from pictures collected with a Multi-Angle Snowflake Camera, Atmospheric Measurement Techniques, 10, 1335, https://doi.org/10.5194/amt-10-1335-2017, 2017.

Rasmussen, R., Dixon, M., Hage, F., Cole, J., Wade, C., Tuttle, J., McGettigan, S., Carty, T., Stevenson, L., Fellner, W., Knight, S., Karplus, E., and Rehak, N.: Weather Support to Deicing Decision Making (WSDDM): A winter weather nowcasting system, Bulletin of the American Meteorological Society, 82, 579–596, https://doi.org/10.1175/1520-0477(2001)082<0579:WSTDDM>2.3.CO;2, 2001.

Rasmussen, R., Baker, B., Kochendorfer, J., Meyers, T., Landolt, S., Fischer, A. P., Black, J., Thériault, J. M., Kucera, P., Gochis, D., et al.: How well are we measuring snow: The NOAA/FAA/NCAR winter precipitation test bed, Bulletin of the American Meteorological Society, 93, 811–829, https://doi.org/10.1175/BAMS-D-11-00052.1, 2012.

Ritsche, M. T.: ARM Surface Meteorology Systems Handbook, techreport DOE/SC-ARM/TR-086, U. S. Department of Energy, Office of Science, https://doi.org/10.2172/1019409, 2011.

Schaer, M., Praz, C., and Berne, A.: Identification of blowing snow particles in images from a multi-angle snowflake camera, The Cryosphere, 14, 367–367, https://doi.org/10.5194/tc-2018-248, 2020.

Schirle, C. E., Cooper, S. J., Wolff, M. A., Pettersen, C., Wood, N. B., L'Ecuyer, T. S., Ilmo, T., and Nygård, K.: Estimation of Snowfall Properties at a Mountainous Site in Norway Using Combined Radar and In Situ Microphysical Observations, Journal of Applied Meteorology and Climatology, 58, 1337–1352, https://doi.org/10.1175/JAMC-D-18-0281.1, 2019.

Shkurko, K., Talaei, A., Garrett, T., and Gaustad, K.: Multi-Angle Snowflake Camera Particle Analysis Value-Added Product, Tech. rep., DOE Office of Science Atmospheric Radiation Measurement (ARM) Program, 2018.

Shupe, M. D., Kollias, P., Persson, P. O. G., and McFarquhar, G. M.: Vertical motions in Arctic mixed-phase stratiform clouds, Journal of the Atmospheric Sciences, 65, 1304–1322, https://doi.org/10.1175/2007JAS2479.1, 2008.

Stuefer, M. and Bailey, J.: Multi-Angle Snowflake Camera Instrument Handbook, Tech. rep., DOE Office of Science Atmospheric Radiation Measurement (ARM) Program, https://doi.org/10.2172/1261185, 2016.

The Hive: University of Utah Research Data Repository: Corrected liquid water path data and *mascpy* code, 2016-12-08 to 2019-11-25. Compiled by K. E. Fitch and T. J. Garrett, University of Utah, Salt Lake City, Utah, USA. Data set processed by Maximilian Maahn, Colorado University, Boulder, Colorado, USA. Code written by K. Shkurko et al., Particle Flux Analytics, Inc., https://doi.org/10.7278/S50DVA5JK2PD, 2020a.

The Hive: University of Utah Research Data Repository: MATLAB code for “Numerical simulations and Arctic observations of surface wind effects on Multi-Angle Snowflake Camera measurements", 2012-05-21 to 2020-07-19. Compiled by K. E. Fitch and T. J. Garrett, University of Utah, Salt Lake City, Utah, USA., https://doi.org/10.7278/S50DQTX9K7QY, 2020b.

Thompson, G., Field, P. R., Rasmussen, R. M., and Hall, W. D.: Explicit forecasts of winter precipitation using an improved bulk microphysics scheme. Part II: Implementation of a new snow parameterization, Monthly Weather Review, 136, 5095–5115, https://doi.org/10.1175/2008MWR2387.1, 2008.

Thériault, J. M., Rasmussen, R., Ikeda, K., and Landolt, S.: Dependence of snow gauge collection efficiency on snowflake characteristics, Journal of Applied Meteorology and Climatology, 51, 745–762, https://doi.org/10.1175/JAMC-D-11-0116.1, 2012.

Thériault, J. M., Rasmussen, R., Petro, E., Trépanier, J.-Y., Colli, M., and Lanza, L. G.: Impact of wind direction, wind speed, and particle characteristics on the collection efficiency of the Double Fence Intercomparison Reference, Journal of Applied Meteorology and Climatology, 54, 1918–1930, https://doi.org/10.1175/JAMC-D-15-0034.1, 2015.

Vignon, E., Besic, N., Jullien, N., Gehring, J., and Berne, A.: Microphysics of snowfall over coastal East Antarctica simulated by Polar WRF and observed by radar, Journal of Geophysical Research: Atmospheres, 124, 11 452–11 476, https://doi.org/10.1029/2019JD031028, 2019.

Vivekanandan, J., Adams, W., and Bringi, V.: Rigorous approach to polarimetric radar modeling of hydrometeor orientation distributions, Journal of Applied Meteorology, 30, 1053–1063, https://doi.org/10.1175/1520-0450(1991)030%3C1053:RATPRM%3E2.0.CO;2, 1991.

Vivekanandan, J., Bringi, V. N., Hagen, M., and Meischner, P.: Polarimetric radar studies of atmospheric ice particles, IEEE Transactions on Geoscience and Remote Sensing, 32, 1–10, https://doi.org/10.1109/36.285183, 1994.

Voth, G. A. and Soldati, A.: Anisotropic particles in turbulence, Annual Review of Fluid Mechanics, 49, 249–276, https://doi.org/10.1146/annurev-fluid-010816-060135, 2017.

Widener, K., Bharadwaj, N., and Johnson, K.: Ka-band ARM Zenith Radar (KAZR) instrument handbook, Tech. rep., DOE Office of Science Atmospheric Radiation Measurement (ARM) Program, https://doi.org/10.2172/1035855, 2012.

Wilks, D. S.: Statistical Methods in the Atmospheric Sciences, vol. 100 of *International Geophysics Series*, Elsevier Academic Press, Amsterdam, 3rd edn., 2011.

Wolff, M., Isaksen, K., Petersen-Øverleir, A., Ødemark, K., Reitan, T., and Brækkan, R.: Derivation of a new continuous adjustment function for correcting wind-induced loss of solid precipitation: results of a Norwegian field study, Hydrology and Earth System Sciences, 19, 951, https://doi.org/10.5194/hess-19-951-2015, 2015.

Yang, D., Metcalfe, J., Goodison, B., and Mekis, E.: True snowfall: An evaluation of the double fence intercomparison reference gauge, in: Proc. 50th Eastern Snow Conference/61st Western Snow Conference, pp. 105–111, 1993.

Yang, D., Kane, D., Zhang, Z., Legates, D., and Goodison, B.: Bias corrections of long-term (1973-2004) daily precipitation data over the northern regions, Geophysical Research Letters, 32, https://doi.org/10.1029/2005GL024057, 2005.